

## THE CARNEGIE-IRVINE GALAXY SURVEY. III. THE THREE-COMPONENT STRUCTURE OF NEARBY ELLIPTICAL GALAXIES

SONG HUANG (黄松)<sup>1,2,3</sup>, LUIS C. HO<sup>2</sup>, CHIEN Y. PENG<sup>4</sup>, ZHAO-YU LI (李兆聿)<sup>5</sup>, AND AARON J. BARTH<sup>6</sup>

<sup>1</sup> School of Astronomy and Space Science, Nanjing University, Nanjing 210093, China

<sup>2</sup> The Observatories of the Carnegie Institution for Science, 813 Santa Barbara Street, Pasadena, CA 91101, USA

<sup>3</sup> Key Laboratory of Modern Astronomy and Astrophysics, Nanjing University, Nanjing 210093, China

<sup>4</sup> Giant Magellan Telescope Organization, 251 South Lake Avenue, Suite 300, Pasadena, CA 91101, USA

<sup>5</sup> Key Laboratory for Research in Galaxies and Cosmology, Shanghai Astronomical Observatory, Chinese Academy of Sciences,

80 Nandan Road, Shanghai 200030, China

<sup>6</sup> Department of Physics and Astronomy, 4129 Frederick Reines Hall, University of California, Irvine, CA 92697-4575, USA

Received 2012 October 9; accepted 2012 December 10; published 2013 March 6

### ABSTRACT

Motivated by recent developments in our understanding of the formation and evolution of massive galaxies, we explore the detailed photometric structure of a representative sample of 94 bright, nearby elliptical galaxies, using high-quality optical images from the Carnegie-Irvine Galaxy Survey. The sample spans a range of environments and stellar masses, from  $M_* = 10^{10.2}$  to  $10^{12.0} M_\odot$ . We exploit the unique capabilities of two-dimensional image decomposition to explore the possibility that local elliptical galaxies may contain photometrically distinct substructure that can shed light on their evolutionary history. Compared with the traditional one-dimensional approach, these two-dimensional models are capable of consistently recovering the surface brightness distribution and the systematic radial variation of geometric information at the same time. Contrary to conventional perception, we find that the global light distribution of the majority ( $\gtrsim 75\%$ ) of elliptical galaxies is not well described by a single Sérsic function. Instead, we propose that local elliptical galaxies generically contain three subcomponents: a compact ( $R_e \lesssim 1$  kpc) inner component with luminosity fraction  $f \approx 0.1\text{--}0.15$ ; an intermediate-scale ( $R_e \approx 2.5$  kpc) middle component with  $f \approx 0.2\text{--}0.25$ ; and a dominant ( $f = 0.6$ ), extended ( $R_e \approx 10$  kpc) outer envelope. All subcomponents have average Sérsic indices  $n \approx 1\text{--}2$ , significantly lower than the values typically obtained from single-component fits. The individual subcomponents follow well-defined photometric scaling relations and the stellar mass–size relation. We discuss the physical nature of the substructures and their implications for the formation of massive elliptical galaxies.

**Key words:** galaxies: elliptical and lenticular, cD – galaxies: formation – galaxies: photometry – galaxies: structure

**Online-only material:** color figures, figure set, machine-readable table

### 1. INTRODUCTION

The formation and evolution of massive elliptical galaxies, as fundamentally important areas in astrophysics, are extensively studied using different observational constraints. Among them, the photometric analysis of their morphological structure remains one of the most efficient and straightforward methods. Since different physical processes can result in different stellar configurations, the surface brightness distribution of a galaxy, as the first-order proxy of the underlying stellar mass distribution, provides an important archaeological record of its evolutionary history.

With their nearly featureless morphologies, elliptical galaxies traditionally have been viewed as structurally simple objects. Historically, the surface brightness profile of luminous elliptical galaxies was described by an  $R^{1/4}$  law (de Vaucouleurs 1948, 1953). This simple profile reflects the high central concentration and large radial extension of the light distribution of massive elliptical galaxies. As an empirical surface brightness model, de Vaucouleurs profile was embraced by different theories for elliptical galaxy formation. Both the dissipational monolithic collapse model (e.g., Larson 1974) and the initially dissipationless disk merger model (e.g., van Albada 1982; Carlberg 1986) predicted that the density profile of the final product should be very similar to the  $R^{1/4}$  law. With the advent of more accurate photometric data, however, the surface brightness profile of elliptical galaxies was found to deviate systematically from

de Vaucouleurs' profile (Kormendy 1977; King 1978; Lauer 1985). These observations showed that elliptical galaxies have a variety of inner profiles that cannot be accommodated by de Vaucouleurs' law.

Beginning in the late 1980s, it was realized that the more flexible  $R^{1/n}$  Sérsic (1968) profile does a much better job of describing the surface brightness profile of elliptical galaxies (Capaccioli 1989; Caon et al. 1993). Over a large radial range, nearby elliptical galaxies were found to be well fit by Sérsic profiles with  $2.5 \lesssim n \lesssim 10$  (e.g., Caon et al. 1994; Bertin et al. 2002; Kormendy et al. 2009, hereinafter K09). Compared with other types of galaxies, ellipticals have significantly larger Sérsic indices, reflecting their high degree of central concentration. As the detailed properties of the Sérsic function became better understood, both theoretically (Ciotti 1991; Hjorth & Madsen 1995; Ciotti & Bertin 1999; Lima Neto et al. 1999) and observationally (Graham & Driver 2005), a variety of studies have explored empirical correlations between the Sérsic index and other key structural parameters (e.g., Caon et al. 1993; Trujillo et al. 2001; Graham et al. 2005). Modern numerical simulations of galaxy formation that invoke either dissipational monolithic collapse (Nipoti et al. 2006) or dissipational merging (Aceves et al. 2006; Naab & Trujillo 2006) can recover the variety of Sérsic shapes observed in ellipticals.

Neither monolithic collapse nor dissipational mergers provide an adequate description of the full evolutionary process of massive elliptical galaxies. Recent observations show that

massive, quiescent early-type galaxies have been in place since  $z \approx 2.5$  (Cimatti et al. 2004, 2008; McCarthy et al. 2004). High-redshift massive galaxies have a great diversity in properties. Of particular interest is the population of “red nuggets,” which appear to be nascent, evolutionary precursors of local giant ellipticals. On average, these quiescent galaxies have smaller size (Daddi et al. 2005; Trujillo et al. 2006; Toft et al. 2007; van der Wel et al. 2008; van Dokkum et al. 2008, 2009; Damjanov et al. 2009; Cassata et al. 2010, 2011; Szomoru et al. 2012) and possibly higher central stellar velocity dispersion (Cappellari et al. 2009; Cenarro & Trujillo 2009; van Dokkum et al. 2009; Onodera et al. 2010; van de Sande et al. 2011) than local elliptical galaxies of the same stellar mass. On average the massive early-type galaxy population appears to require a doubling in stellar mass and tripling in size during the epoch between  $z = 2.0$  and 1.0 (van Dokkum et al. 2010; see also Cimatti et al. 2012). Stacking analysis of large samples of early-type galaxies at different redshift bins (Bezanson et al. 2009; van Dokkum et al. 2010) and deep near-infrared images of individual objects (Szomoru et al. 2012) reveal that high-redshift red nuggets differ from local ellipticals in two ways: They lack an extended outer envelope while at the same time their inner stellar mass density is higher. These observational constraints strongly challenge theoretical scenarios wherein either dissipational collapse or gas-rich major mergers dominate during the main phases of elliptical galaxy formation. Dissipational processes lead to greater central concentration, not envelope building as required by the observed dramatic size growth. Whatever the mechanism, there does not appear to be a high enough rate of major mergers to do the job since  $z \approx 2.0$  (Williams et al. 2011; Nipoti et al. 2012).

A variety of different physical explanations have been proposed to explain the above recent observations, including dry (minor) mergers (Naab et al. 2007, 2009), fading gas-rich mergers (Hopkins et al. 2009b), mergers plus selection effects (van der Wel et al. 2009), and feedback by active galactic nuclei (Fan et al. 2008). Among these models, the two-phase formation scenario of Oser et al. (2010, 2012; see also Johansson et al. 2012) seems particularly promising in matching a number of observational constraints (Coccato et al. 2010; Greene et al. 2012; Papovich et al. 2012; Romanowsky et al. 2012), numerical simulations (Gabor & Davé 2012), and semi-analytic models (Khochfar et al. 2011). Under this picture, the initial evolution phase at high redshifts ( $z \leq 3$ ) is dominated by in situ star formation induced by cold-phase accretion and gas-rich mergers, while later evolution is instead dominated by dissipationless processes such as dry (minor) mergers and hot-phase accretion. It is the second phase that is responsible for the build-up of the low-density outer envelope of local massive ellipticals.

Elliptical galaxies are not as simple as they seem. Fine structures such as shells and tidal features have been identified in some ellipticals even before the era of CCD photometry (Malin 1979; Schweizer 1980, 1982; Malin & Carter 1983). Deep, modern images of nearby elliptical galaxies show that the majority of them, in fact, contain extended, low-surface brightness features consistent with a tidal origin (Tal et al. 2009). On smaller scales, dust absorption features, including regular dust lanes, are frequently visible (Lauer 1985; Ebneter et al. 1988), as are embedded nuclear stellar disks (Carter 1978; Bender 1988; Franx et al. 1989; Peletier et al. 1990; Ledo et al. 2010). These substructures are often attributed to merger or accretion events. Even when the overall light distribution of ellipticals appears smooth, it is not uncommon to see isophotal

twists (Kormendy 1982; Fasano & Bonoli 1989), which often cannot be explained as an artifact of dust absorption. Nieto et al. (1992) suggested that structural subcomponents may give rise to the isophotal twists observed in ellipticals.

The innermost regions of nearby elliptical galaxies contain photometrically distinct components. This was recognized even from ground-based images (Lauer 1985; Kormendy 1985) and has been fully elaborated with higher resolution data from *Hubble Space Telescope* (*HST*; e.g., Jaffe et al. 1994; Lauer et al. 1995, 2007; Côté et al. 2006; Ferrarese et al. 2006). Depending on the relative steepness of the inner luminosity profile compared to the global one, the central regions of nearby elliptical galaxies have been classified into “core” and “power law” (or “extra-light”) types, whose incidence depends strongly on galaxy luminosity (Faber et al. 1997; Lauer et al. 2007; K09): steep power-law cusps are found mostly in lower-luminosity systems, whereas lower density cores reside exclusively in the most massive, luminous ellipticals. Various empirical functions have been used to describe these inner “deviations” of the surface brightness profile. The most popular has been the “Nuker” law (Lauer et al. 1995), but other forms have been used (Ferrarese et al. 1994; Graham et al. 2003; Trujillo et al. 2004; Côté et al. 2006; Hopkins et al. 2009a).

At the another extreme end in scale, the most luminous members of the elliptical galaxy family are known to have extended stellar envelopes (Morgan & Lesh 1965; Oemler 1974; Schombert 1986). This phenomenon is especially common for the brightest cluster galaxies. It is also known that in certain cases these extended envelopes around the brightest cluster galaxies can have a multiple-component structure (e.g., NGC 3311, the brightest cluster galaxy in the Hydra I cluster; Arnaboldi et al. 2012) and/or an off-center appearance (e.g., the brightest cluster galaxy of Abell 1651; González et al. 2005). Outer envelopes that cannot be fitted well using a Sérsic profile often yield a larger Sérsic index in a single-component fit. Some authors have adopted more complex profiles to account for this additional structure (e.g., Graham et al. 1996; González et al. 2005; Zibetti et al. 2005; Seigar et al. 2007). In general, however, ellipticals with extended envelopes are considered to be rare, special cases.

Despite the abundant evidence that elliptical galaxies do have structural complexities on different scales, it is still customary to regard the bulk of the stellar surface brightness distribution—excluding the central “deviations”—in these systems as a single entity described by a single Sérsic profile. In light of recent observational and theoretical developments on the formation and evolution of massive galaxies, we believe that it would be instructive to take a fresh look at this problem. We take as our starting point a collection of high-quality optical images available for a relatively large, well-defined sample of nearby, bright elliptical galaxies selected from the Carnegie-Irvine Galaxy Survey<sup>7</sup> (CGS; Ho et al. 2011, Paper I; Li et al. 2011, Paper II). We carefully analyze these data with a two-dimensional (2D) image decomposition method, demonstrating that the majority of nearby ellipticals contain three well-defined subcomponents. The physical implications of these substructures are discussed in a companion paper by S. Huang et al. (2013, in preparation).

This paper is organized as follows. Section 2 gives a brief overview of the elliptical galaxy sample, the observations, and basic data reduction procedures. In Section 3, we give a description of our 2D image decomposition method, sky

<sup>7</sup> <http://cgs.obs.carnegiescience.edu>

background measurement, and other details related to the model fitting. Section 4 summarizes the main properties of the model parameters, the distributions of key structural parameters, and several important scaling relations. The physical nature of the galaxy subcomponents is discussed in Section 5 within the framework of elliptical galaxy formation. Section 6 briefly mentions interesting future directions, ending with a summary in Section 7.

As in other papers in the CGS series, we assume  $H_0 = 73 \text{ km s}^{-1} \text{ Mpc}^{-1}$ ,  $\Omega_m = 0.27$ , and  $\Omega_\Lambda = 0.73$ .

## 2. SAMPLE AND DATA

CGS is a long-term project to investigate the photometric and spectroscopic properties of nearby galaxies (Ho et al. 2011). The first part of the project is an optical photometric survey of galaxies that span the full range of the Hubble sequence in the local universe. The sample consists of a statistically complete sample of 605 galaxies drawn from the Third Reference Catalogue of Bright Galaxies (RC3; de Vaucouleurs et al. 1991) and is defined by  $B_T \leq 12.9$  mag and  $\delta < 0^\circ$ . As most of the galaxies are nearby (median  $D_L = 24.9 \text{ Mpc}$ ), luminous (median  $M_{B_T} = -20.2$  mag, corrected for Galactic extinction), and angularly large (median  $B$ -band isophotal diameter  $D_{25} = 3.3'$ ), it is feasible to obtain high signal-to-noise ratio images with good spatial resolution. Visually selecting a sample of “pure” ellipticals, even for nearby galaxies, is challenging. Ellipticals can be easily confused with face-on, unbarred S0 galaxies. We begin with the 103 galaxies in CGS originally classified as ellipticals in the RC3. Nine galaxies were rejected for various reasons: NGC 6758 does not have sufficient data; ESO 356-G004 (Fornax) is a spheroidal galaxy; ESO 495-G021 (Henize 2-10) is a very active starbursting dwarf; and six (NGC 3309, 3311, 4105, 5090, 5193, 7176) are in merging or strongly interacting systems. An additional object, NGC 2974, is severely contaminated by a nearby bright star, which makes image decomposition very unreliable; we do not reject it from the final sample, but we exclude it from detailed image decomposition. The final sample considered in this paper contains 94 galaxies deemed to be ellipticals in the RC3, whose morphological assignments were based on visual classification. As will be discussed later, a few of the galaxies turn out to be misclassified S0s. We do not remove these a priori, as we are interested in knowing how well we can separate them using our image decomposition method, in light of recent kinematic studies (Emsellem et al. 2007; Cappellari et al. 2011a) that have blurred the morphological boundary between E and S0 galaxies. In any case, the small number of potentially misclassified Es does not change any of our main statistical conclusions.

Although our final sample consists of relatively isolated ellipticals, seven of them (IC 3370, NGC 596, 1340, 1700, 2865, 3923, 5018) clearly show shell or tidal features in their  $V$ -band images. NGC 3923, in fact, is a prototypical Type I shell elliptical galaxy (Malin & Carter 1980), and the others are known in the literature as post-starburst or “young” ellipticals. Using looser criteria, our visual examination of the images reveals another seven that may show signs of tidal or shell-like structures, bringing the total frequency of Es with such features to  $\sim 15\%$  within CGS. Given the modest surface brightness sensitivity and limited field of view (FoV) of our images, this percentage is, of course, only a lower limit. Some of our galaxies overlap with those in the OBEY survey<sup>8</sup>

(Tal et al. 2009), whose images have a larger FoV and are  $\sim 2$  mag deeper in  $V$ . It is interesting to note that, after applying contrast enhancement techniques (e.g., adaptive histogram equalization; Peng et al. 2002b), we can detect in the CGS  $V$ -band images most of the low-surface brightness features seen in the OBEY data. We will not discuss these low-surface brightness features further in this paper. We simply note that none of these low-level features significantly impact our image decomposition of the light distribution in the main body of the galaxy.

Figure 1 presents a montage of the three-color, star-cleaned images of the final sample of 94 elliptical galaxies. The galaxies are arranged in the order of decreasing absolute  $B$ -band absolute magnitude. Some basic properties of the sample, compared to the parent CGS, are shown in Figure 2. According to the environment information presented in Paper I, most (80%) of the Es live in group-like environments; only six are in a cluster (Fornax), and 14 can be considered field galaxies. Overall, the CGS objects form a representative sample of bright, local Es. Figure 3 illustrates that the CGS Es populate a well-defined red sequence and define a relatively tight Faber & Jackson (1976) relation. Our sample uniformly populates the luminosity–ellipticity plane (Figure 4), as does other well-studied, homogeneous samples of elliptical galaxies, such as those contained in the Atlas<sup>3D</sup> project (Cappellari et al. 2011b; see also de Zeeuw et al. 2002).

Papers I and II give full details of the observations and data reductions, which will not be repeated here. The overall quality of the CGS images is quite high, both in terms of resolution (pixel scale  $0''.259$ ; median seeing  $\sim 1''$ ) and FoV ( $8.9' \times 8.9'$ ). The surface brightness sensitivity of the images, limited principally by the accuracy of sky subtraction, reaches  $\sim 27.5, 26.9, 26.4$ , and  $25.3$  mag arcsec $^{-2}$  in the  $B, V, R$ , and  $I$  bands, respectively. This work will only use the  $V$ -band images. Although the  $V$  band is not the best tracer of the underlying old stellar population, it suffers the least from the “red halo” effect on the point-spread function (PSF; Appendix A; also see Michard 2002 and Wu et al. 2005). Compared with the  $R$  and  $I$  bands, the  $V$  band has an additional advantage of having lower sky background brightness. This enables more accurate sky subtraction and allows us to probe to lower surface brightnesses.

## 3. TWO-DIMENSIONAL DECOMPOSITION

The vast majority of previous studies of the photometric structure of elliptical galaxies have relied on one-dimensional (1D) analysis of their light distribution. Apart from small deviations near the center, the radial profile of ellipticals, especially when viewed under ground-based resolutions, is usually modeled as a single component,<sup>9</sup> often fit with de Vaucouleurs’ (1948) law or a Sérsic (1968) function. Although this approach is straightforward and generally suffices to describe the overall global structure, it is not very effective in isolating individual subcomponents, should they exist, because it cannot easily take advantage of the geometric information encoded in the 2D image that can help to break the degeneracy between overlapping subcomponents. In this study, we will employ 2D image decomposition to study the detailed photometric structure of the CGS ellipticals. We relax the assumption that the main body of ellipticals is a single-component object. We take advantage of our high-quality images and a 2D fitting technique to explore more complex, multi-component models.

<sup>8</sup> <http://www.astro.yale.edu/okey/>

<sup>9</sup> An exception are brightest cluster galaxies, which have long been recognized to contain an additional extended envelope (e.g., Schombert 1986).

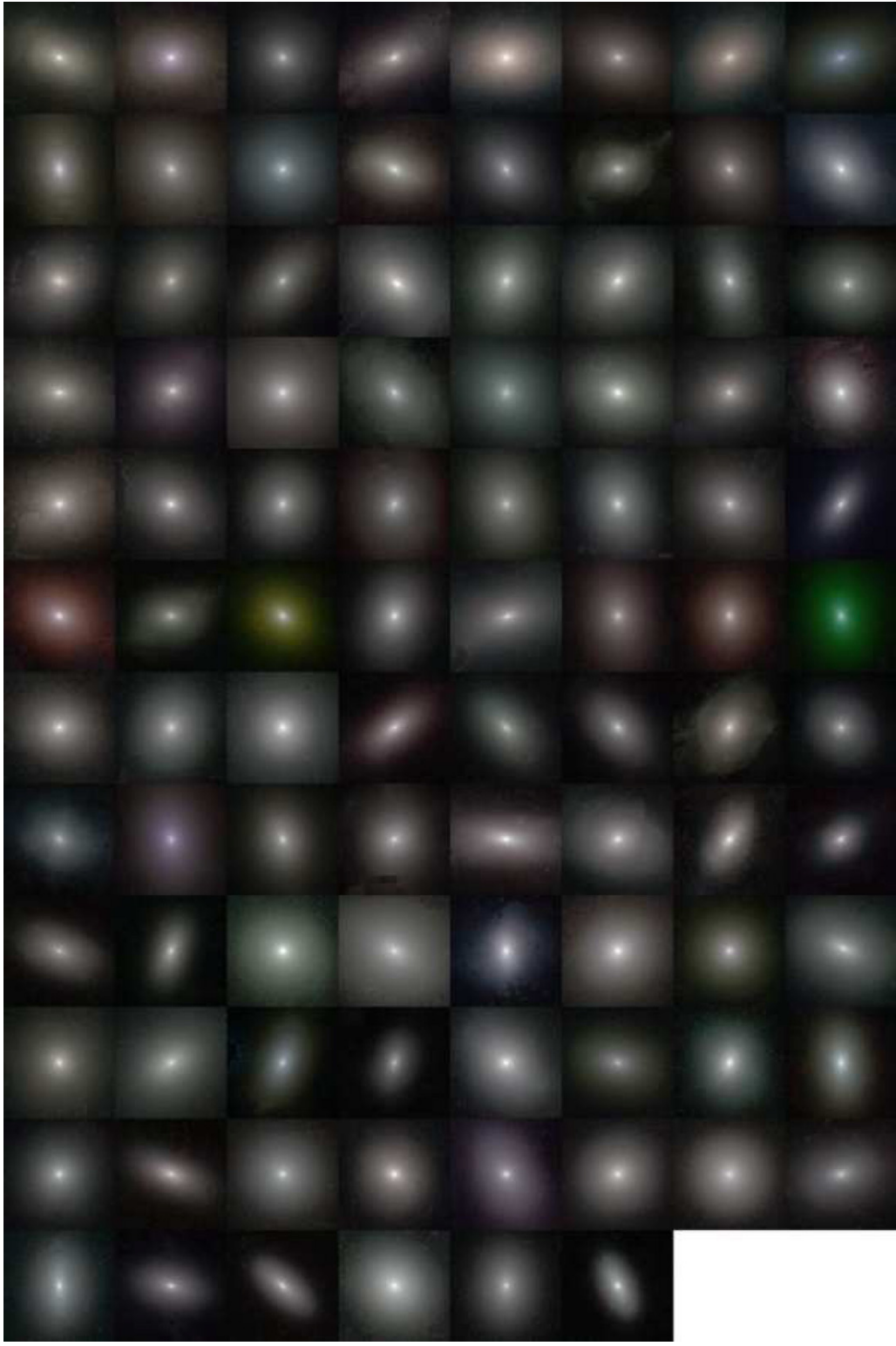


**Figure 1.** Mosaic of three-color, star-cleaned images of the 94 elliptical galaxies in our sample. The dimensions of each panel vary, with each side corresponding to  $1.5 D_{25}$ ; north is up and east is to the left. From upper left to bottom right, the galaxies are arranged in the order of decreasing  $M_{B_T}$ . The image colors here are not directly related to the actual galaxy colors, and the discrepant colors are seen in a few objects having data of lower signal-to-noise ratio.

(A color version of this figure is available in the online journal.)

Our analysis uses the most recent version of GALFIT<sup>10</sup> (Peng et al. 2002a, 2010), a flexible fitting algorithm designed to perform 2D decomposition of galaxy images. GALFIT can fit

an arbitrary number and combination of parametric functions, and version 3.0 has the additional capability of modeling non-axisymmetrical structures such as bars, spiral arms, and tidal features. In the case of elliptical galaxies treated in this study, we consider only the Sérsic function. We adopt this function not

<sup>10</sup> <http://users.obs.carnegiescience.edu/peng/work/galfit>

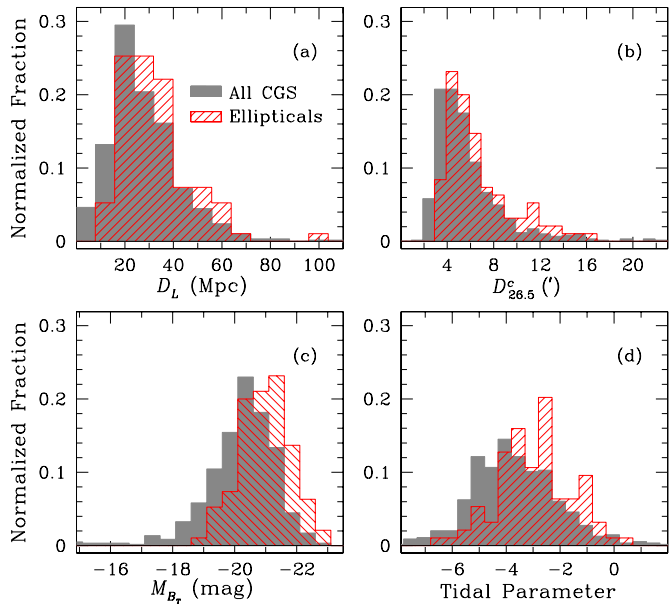


**Figure 2.** Normalized distributions of several properties for the whole CGS sample and the 94 elliptical galaxies sample in this work: (a) luminosity distance; (b) corrected isophotal diameter corresponding to an  $I$ -band surface brightness of 26.5 mag arcsec $^{-2}$ ; (c)  $B$ -band absolute total magnitude, corrected for Galactic extinction; (d) tidal parameter. The detailed definition of the tidal parameter can be found in Paper I. All the data are taken from Paper I.

(A color version of this figure is available in the online journal.)

because of any physical motivation, but rather because it has enough flexibility to accommodate most of the main structural components in galaxies. Being widely used in the literature, it also provides a convenient basis for comparison with published results.

The Sérsic profile has the following form:

$$\mu(R) = \mu_e \exp \left[ -\kappa \left( \left( \frac{R}{R_e} \right)^{1/n} - 1 \right) \right]. \quad (1)$$

It has seven free parameters: the central position  $x_0$  and  $y_0$ , the profile shape parameter  $n$ , effective radius  $R_e$ , surface brightness  $\mu_e$  at  $R_e$ , axial ratio  $b/a$ , and position angle PA. The parameter  $\kappa$  is a variable that depends on  $n$ .

Galaxy isophotes are seldom perfect ellipsoids. Even in 1D analysis, it is common practice to improve the fits of elliptical isophotes with the addition of perturbations in the form of Fourier modes (e.g., Jedrzejewski 1987). GALFIT 3.0 now allows Fourier modes to be added to 2D image fitting. As shown in Peng et al. (2010), Fourier modes enable one to model a wide range of realistic features, including lopsidedness, boxy or disky shapes, and even more complicated structures often seen in actual galaxy images. The Fourier modes in GALFIT have many potential applications. For this study, we will focus on just two: the  $m = 1$  mode to quantify the overall degree of asymmetry in the galaxy and the  $m = 4$  mode to simulate boxy or disky isophotes. We turn on these modes only after we have first achieved an overall satisfactory model without them, for the purposes of further improving the residuals.

### 3.1. Sky Background

An accurate measurement of the sky background is crucial for our analysis, as we are interested in modeling structures covering a wide dynamic range in surface brightness, including

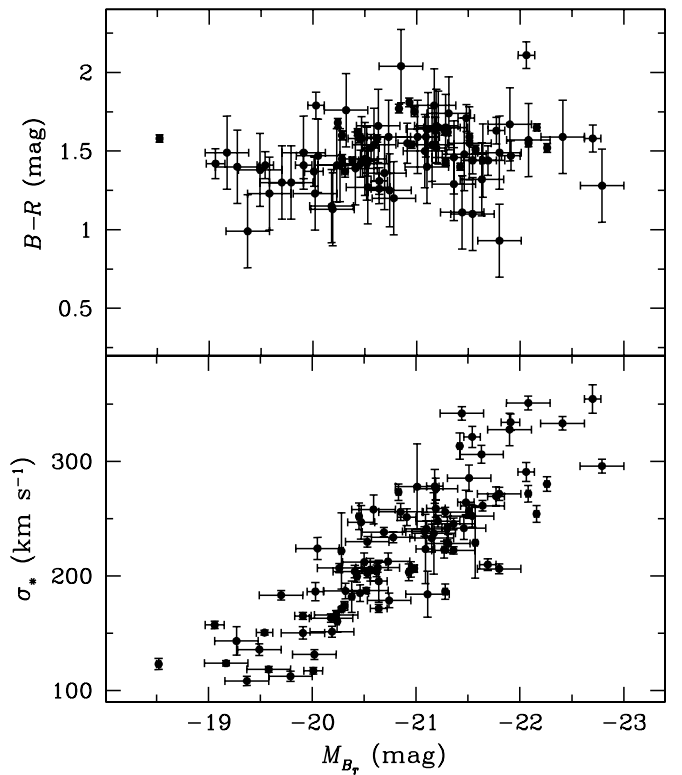


**Figure 3.** Color–magnitude (top) and the Faber–Jackson (bottom) relation for the elliptical galaxies in our sample. The total  $B$ -band absolute magnitude is used to represent the luminosity.

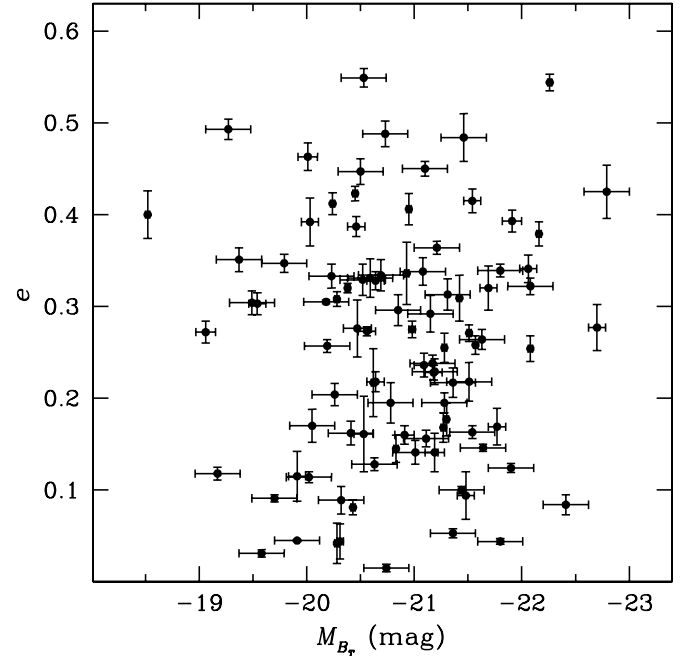


**Figure 4.** Distribution of our sample of elliptical galaxies on the plane of total luminosity and average ellipticity as described in Paper II. The uniform distribution on this plane indicates that our sample is representative of the elliptical galaxy population within this luminosity range.

faint features at large radii. Although the FoV of CGS images is large enough to cover the full extent of most galaxies, some ellipticals have sufficiently large angular sizes ( $D_{25} > 7'$ ) that it would be very difficult to measure accurate sky backgrounds. An additional complication, as explained in Papers I and II, is

that some of the CGS images contain residual flat-field errors that imprint low-level, large-scale variations in the background. Although the strategy outlined in [Paper II](#) can recover the sky background to an accuracy of  $\sim 0.6\%$  for relatively compact galaxies, it is likely that the sky determination is more uncertain for the more extended sources that fill an appreciable portion of the detector. The sky level for the angularly large galaxies was estimated in a model-dependent manner by fitting the outer portions of the light profile with a Sérsic function, and the uncertainty of the sky was estimated from a set of empirical calibrations determined from simulated images in which the galaxy occupies different relative fractions of the FoV.

Here, for the elliptical galaxy sample, we explore an alternative method to measure the sky background and its uncertainty, one that can be applied uniformly and consistently across the whole sample. As described in greater detail in Appendix B, we determine the sky from multi-component fits to the entire image, using as many Sérsic components as necessary to achieve a good model for the galaxy, while simultaneously solving for the sky as an additional component. We adopt as the final sky level the average of the sky values from all the acceptable fits. The uncertainty in the final sky value is estimated from the amplitude of the background fluctuations in the image, using an empirical relation calibrated from simulated data. For a subset of the more compact galaxies, we verify that this model-dependent estimate of the sky yields results consistent with the more traditional model-independent, direct method of measuring the sky background ([Paper I](#)). Appendix C describes additional checks using a set of Sloan Digital Sky Survey (SDSS) images that do not suffer from FoV limitations.

### 3.2. Model Fitting Procedures

With the sky value and its uncertainty in hand, we fit each galaxy with a series of models, each consisting of one to four Sérsic components. Unlike in the earlier phase of model fitting, wherein the purpose of the multiple components was to solve for the optimal sky value, here we use multiple components to explore the possibility that the galaxy contains real substructure. Our approach is conservative: start simply and slowly, systematically increase the complexity as the data permit. We always begin with a single Sérsic component, and we add additional components, one at a time, after evaluating the residuals and a number of other constraints, as explained in the next section. Here we briefly summarize the main steps of the fitting process.

We start with the exposure time-corrected V-band images, object masks, and empirical PSF images from [Paper I](#). The object masks were created from the segmentation images from Sextractor.<sup>11</sup> After removing the segment for the target elliptical galaxy, the sizes of the rest of the segments were increased according to their brightness to achieve better coverage of the objects that need to be masked. The PSF images were obtained using standard IRAF procedures. Details of the methods for building object masks and PSF images are given in [Paper I](#). The sky value is fixed to the previously determined value, but we allow for an additional tilt to account for a possible residual gradient in the sky. Normally this gradient, if present, is extremely small and does not affect at all the final models.

For the single-component model, the initial guesses for the total magnitude, effective radius, ellipticity, and PA are taken

from [Paper I](#); the Sérsic index is set initially to  $n = 2.5$ . For the multi-component models, reasonable choices for the initial parameters are made based on the best-fit values from the single-component trial, generally letting the inner component assume a larger effective surface brightness and a slightly higher Sérsic index. We require the different components to share the same central position. The Fourier modes are initially turned off.

Next, we carefully inspect the residual image with the original object mask overlaid. In some cases we find that the original object mask needs to be enlarged to better cover the outermost regions of bright objects such as background galaxies, nearby companions, or saturated stars. Occasionally we discover previously unmasked stars directly superposed on the target of interest, often close to the galaxy center. Since these objects can introduce potential uncertainty into the multi-component model, we aggressively masked them out, and we repeat this process until the rest of the image is free of these artifacts.

The final set of models is generated with the updated, refined object mask and with the Fourier modes enabled for each component. We restrict our attention to the  $m = 1$  mode to account for global asymmetry and the  $m = 4$  mode to simulate different isophote shapes. Since the elliptical galaxies in this sample are already known to have little morphological peculiarity, the inclusion of the Fourier modes does not have an effect on the main results; they primarily serve to improve the residuals in the final models.

For each object we perform a series of tests to evaluate the reliability and robustness of the results, to explore the potential degeneracy among different model subcomponents, and to obtain a realistic estimate of the uncertainties of the model parameters. Apart from the best-fitting sky value, we rerun the models with the sky changed to plus and minus the estimated sky uncertainty. We also test the sensitivity of the final models to our choice of input parameters by perturbing the initial parameters to dramatically different values. In general, the models, even those with more than one component, are not very sensitive to the choice of initial parameters, so long as the initial guesses are not wildly off the mark.

The innermost regions of the galaxies pose special challenges. Although our models are convolved with the nominal seeing of the observations (as formally represented by the empirical PSF image), in practice the seeing profile is not known perfectly, and any residual errors in the seeing estimate can lead to significant mismatch between the model and the data. Furthermore, we know from high-resolution studies (e.g., Lauer et al. 1995; Ravindranath et al. 2001) that elliptical galaxies often contain substructure within the central few hundred parsecs. Even for nearby galaxies, this inner substructure is not well resolved with our typical seeing, and failure to account for it in our models could bias our global fits. To evaluate the impact of seeing and unresolved inner substructure, during the model selection process we compare fits with and without a central mask applied. After extensive testing (Appendix D), we conclude that a circular central mask with a radius equal to twice the full width at half-maximum (FWHM) of the PSF is the most appropriate choice for most of the observations. These central masks are used for two purposes in this work. First, for each model, an extra run is performed using exactly the same parameters but with the central mask applied. These tests evaluate the impact from the seeing and the robustness of the central component. Second, to compare with the approach taken by K09 in constructing their 1D single-Sérsic models, we also apply a central mask to

<sup>11</sup> <http://www.astromatic.net/software/sextractor>

**Table 1**  
Best-fit Models

Galaxy	Model	$R_e$ (kpc)	$\mu_e$ (mag arcsec $^{-2}$ )	$M_V$ (mag)	$n$	$e$	PA ( $^{\circ}$ )	$A_L$	$f$	Sky (counts)	EVI
(1)	(2)	(3)	(4)	(5)	(6)	(7)	(8)	(9)	(10)	(11)	(12)
ESO 185-G054	3 Sérsic	0.93	18.83	-20.10	0.98	0.29	117.9	0.02	0.07	155.3	0.42
		2.91	21.21	-19.90	0.41	0.25	119.6	0.04	0.06		
		18.81	23.05	-22.86	2.52	0.27	120.0	0.02	0.87		
ESO 221-G026 <sup>a</sup>	4 Sérsic	0.10	16.61	-17.37	7.84	0.85	5.41	0.04	0.07	147.7	0.53
		0.25	18.58	-17.74	1.04	0.47	6.27	0.01	0.11		
		1.82	21.95	-17.82	0.78	0.72	4.07	0.03	0.11		
		3.03	22.58	-19.81	2.63	0.32	178.3	0.01	0.71		
IC 1459	3 Sérsic	0.60	18.03	-20.13	1.77	0.25	33.11	0.01	0.13	87.46	0.24
		5.69	21.71	-21.47	2.86	0.31	31.48	0.01	0.44		
		10.55	22.98	-21.45	2.53	0.28	59.39	0.03	0.43		
IC 1633	3 Sérsic	1.94	19.18	-21.69	1.93	0.16	106.7	0.00	0.17	120.9	0.89
		8.61	22.36	-21.34	0.75	0.14	144.9	0.05	0.12		
		38.10	23.78	-23.22	1.61	0.30	83.94	0.04	0.70		
IC 2006 <sup>b</sup>	4 Sérsic	0.62	20.81	-17.00	0.48	0.13	42.97	0.01	0.06	135.8	0.03
		1.13	21.09	-19.10	4.45	0.10	39.37	0.01	0.40		
		2.20	21.57	-19.24	0.89	0.13	40.38	0.00	0.45		
		9.73	25.89	-17.50	0.13	0.17	49.59	0.03	0.09		
IC 2311	4 Sérsic	0.32	18.92	-18.84	3.54	0.12	20.70	0.01	0.13	141.3	0.45
		0.46	19.69	-18.05	0.58	0.06	170.6	0.01	0.06		
		1.55	20.91	-19.76	1.04	0.03	45.69	0.01	0.30		
		8.57	24.11	-20.35	1.27	0.05	171.7	0.06	0.51		
IC 2597	3 Sérsic	0.65	19.27	-19.23	1.63	0.23	10.33	0.01	0.13	86.63	0.45
		2.17	23.24	-17.57	0.53	0.09	36.26	0.05	0.03		
		9.43	23.19	-21.22	2.89	0.32	7.96	0.01	0.84		

**Notes.** For models with multiple components, the individual components are listed in the order of increasing effective radius. Column (1) Galaxy name. Column (2) Model name. Column (3) Effective radius. Column (4) Surface brightness at the effective radius. Column (5)  $V$ -band absolute magnitude of the component. Column (6) Sérsic index. Column (7) Ellipticity of the component. Column (8) Position angle. Column (9) Lopsidedness amplitude, as defined by Equation (24) in Peng et al. (2010). Column (10) Luminosity fraction of the component. Column (11) New sky background value. Column (12) Excess variance index.

<sup>a</sup> The galaxy has an edge-on disk-like structure.

<sup>b</sup> The galaxy has a ring-like structure in the outskirts.

<sup>c</sup> Merger remnant.

<sup>d</sup> The galaxy is contaminated by a saturated star.

<sup>e</sup> The adopted model still contains significant residuals.

<sup>f</sup> The galaxy has a central dust lane.

<sup>g</sup> The galaxy is a possible S0 galaxy.

(This table is available in its entirety in a machine-readable form in the online journal. A portion is shown here for guidance regarding its form and content.)

our 2D single-component models. Although the method used to decide the size of the central mask is different between K09 and this paper, we can show that the single-component models in both studies behave consistently on important scaling relations.

### 3.3. Sample Fits

Using procedures described in the above section, a series of models with a different number of components was generated for each galaxy. Therefore, the “best” model needs to be carefully selected for further analysis. For this purpose, a reasonable definition of “best” model is proposed. Also, we design a consistent method to compare these models both qualitatively and quantitatively. This crucial definition and method will be discussed in detail in the next section. But, first, we show a few examples of best-fit models to illustrate the range of typical structures encountered in our sample. The full set of fits for the 94 CGS ellipticals is presented in Appendix E, and a summary of the final, best-fit parameters is given in Table 1.

NGC 5077, a member of a small group, is an elliptical in pair with NGC 5079. The best model, summarized in Figure 5,

consists of a dominant inner ( $R_e = 2.69$  kpc) component with a high Sérsic index ( $n = 3.2$ ) and an extended ( $R_e = 12.3$  kpc), diffuse outer component with  $n = 1.1$ . Both the ellipticity and the PA are reasonably well reproduced, except for the innermost region where the color index maps (Paper II) suggest that there are dust patches. Although the 2D residuals are not very clean, the existence of extended dust structures prevents us from exploring more complex models. Only five galaxies in our sample have two-component models as their best fit. Indeed, the residual patterns of all the two-component models can be improved by introducing additional components, but various complications (e.g., strong contamination from nearby stars or poorly resolved substructure near the nucleus) preclude us from pursuing more complex models.

NGC 720 is a well-studied elliptical galaxy known to have a central disk-like structure (Goudfrooij et al. 1994; Rembold et al. 2002). Its ellipticity gradually increases toward larger radius. Our best-fit model (Figure 6) contains three components: a compact inner component with  $R_e = 0.46$  kpc,  $n = 0.63$ , and luminosity fraction  $f = 0.06$ ; an intermediate-scale disk-like component with  $R_e = 1.38$  kpc,  $n = 1.0$ , and

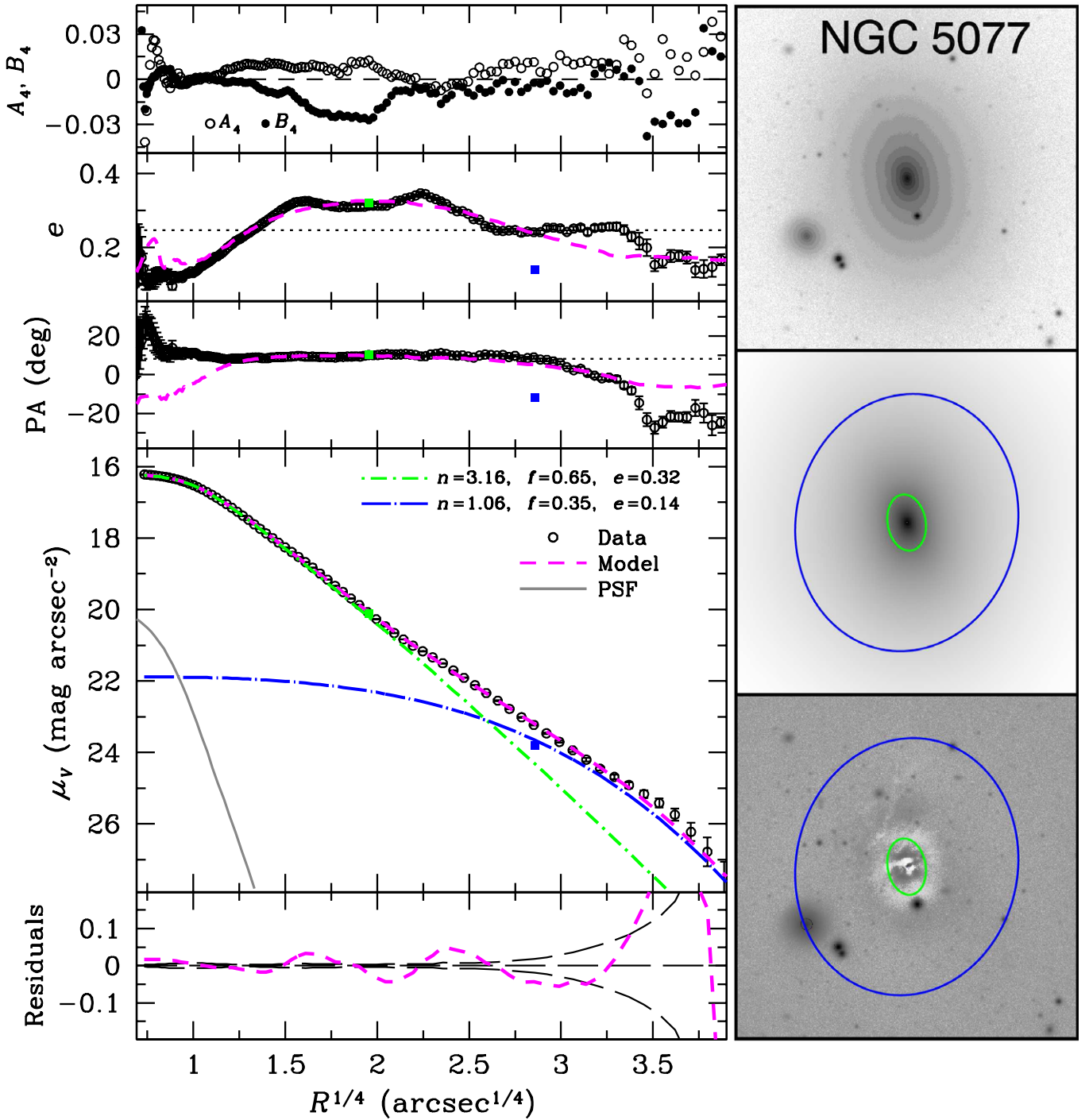


**Figure 5.** Best-fit two-component model of NGC 5077. The right panels display, from top to bottom, images of the original data, the best-fit model, and the residuals; each panel has a dimension of  $2R_{50}$  and is centered on the nucleus. The left panels compare the 1D profiles of the data and the model; from top to bottom, we show the isophotal shape parameters  $A_4$  and  $B_4$ ,  $e$ , PA,  $\mu$ , and the residuals between the data and the model. The observed  $\mu$  profile is extracted with  $e$  and PA fixed to the average value of the galaxy (Paper II), which is indicated by the dotted line in the  $e$  and PA panels. Here, the deviations of the isophotes from perfect ellipses are parameterized by the forth harmonics of the intensity distribution ( $A_4, B_4$ ) as described in Jedrzejewski (1987). Individual subcomponents, each extracted using the geometric parameters generated by GALFIT, are plotted with different line types and colors; the PSF is plotted with arbitrary amplitude. Colored squares on the  $e$ , PA, and  $\mu$  plots mark the ellipticity, position angle, and effective surface brightness of each component. The same color scheme is used in the gray-scale images, where the ellipses trace  $R_{50}$ ,  $e$ , and PA of each component. In the residual plot, the three black dashed lines indicate the position of zero residuals and the level of photometric error.

(A color version of this figure is available in the online journal.)

$f = 0.16$ ; and a dominant outer component with  $R_e = 8.18$  kpc,  $n = 2.4$ , and  $f = 0.78$ . Some residuals can still be seen in the innermost region, but the model in general reproduces well the overall structure of the galaxy, especially its ellipticity profile.

Figure 7 gives another example of an elliptical (NGC 1600) that requires a multi-component model to describe the full radial range captured in our images. Three components give a reasonably good fit, especially when we take into consideration the rather complex ellipticity profile, which cannot be recovered

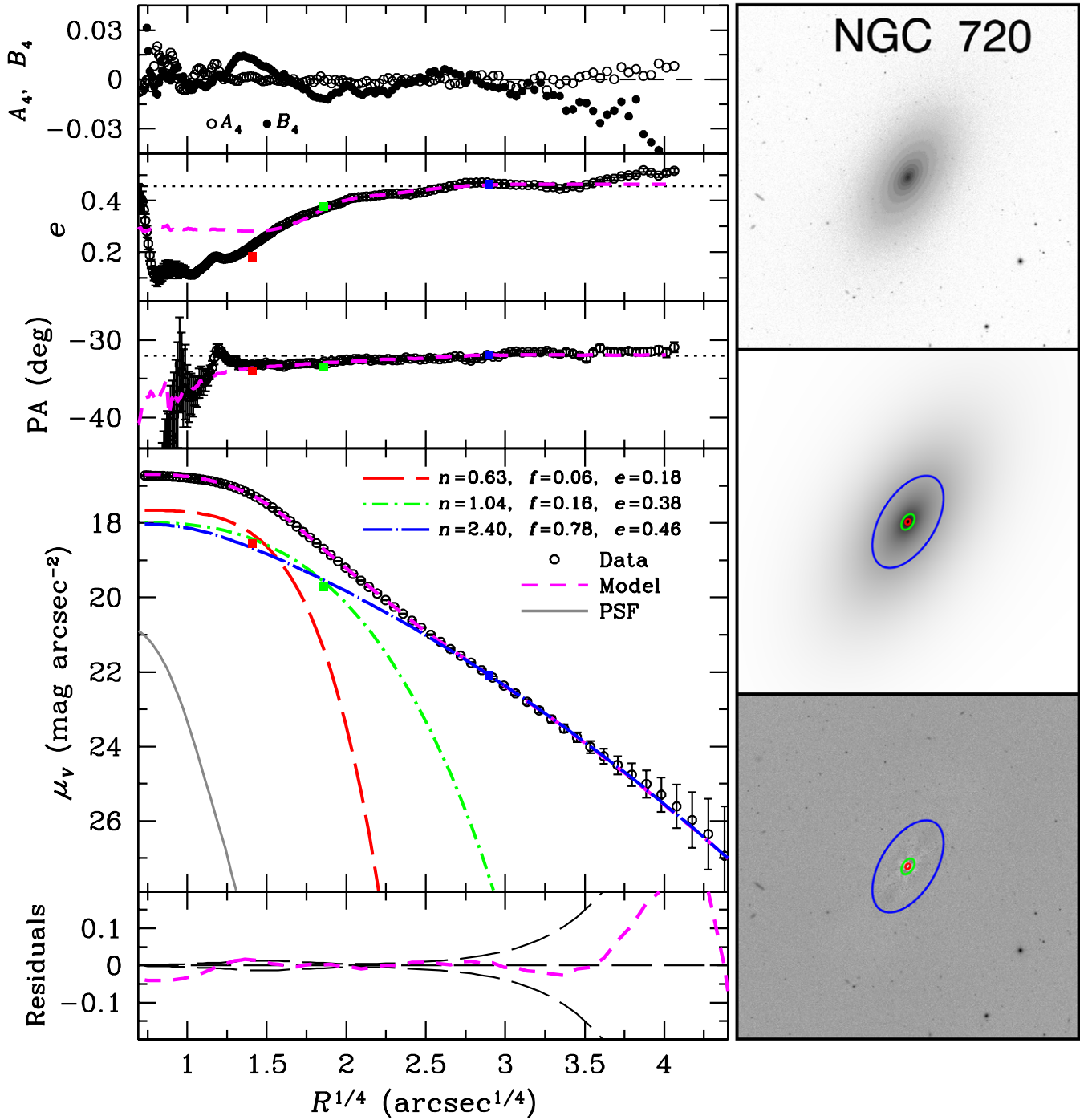


**Figure 6.** Best-fit three-component model for NGC 720. In this and subsequent figures, the inner, middle, and outer component are plotted in red, green, and blue, respectively. All other conventions are the same as in Figure 5.

(A color version of this figure is available in the online journal.)

with either one or two components alone. The constancy of the PA with radius precludes the possibility that the ellipticity changes are induced by isophotal twists. Interestingly, none of the three components has a Sérsic index higher than 1.5; both the middle and outer components formally have  $n < 1$ . Our tests indicate that the three-component structure is robust with respect to changes in the sky background, although the exact value of the Sérsic index for the outer component can vary from  $n = 0.7$  to  $2.1$ .

The above two cases (NGC 720 and NGC 1600) are good examples of the most common configurations encountered in

our survey. Roughly 75% of the sample can be described by a qualitatively similar three-component model. Taking into consideration that many of the galaxies modeled by two components may, in fact, also be better fit with three components, the general picture that emerges from our analysis is that the structure of most nearby ellipticals consists of three photometrically distinct components.

It is often extremely difficult to recognize large-scale sub-components in the 1D azimuthally averaged surface brightness profiles of ellipticals. Different subcomponents, if present, usually have very low relative contrast and blend nearly

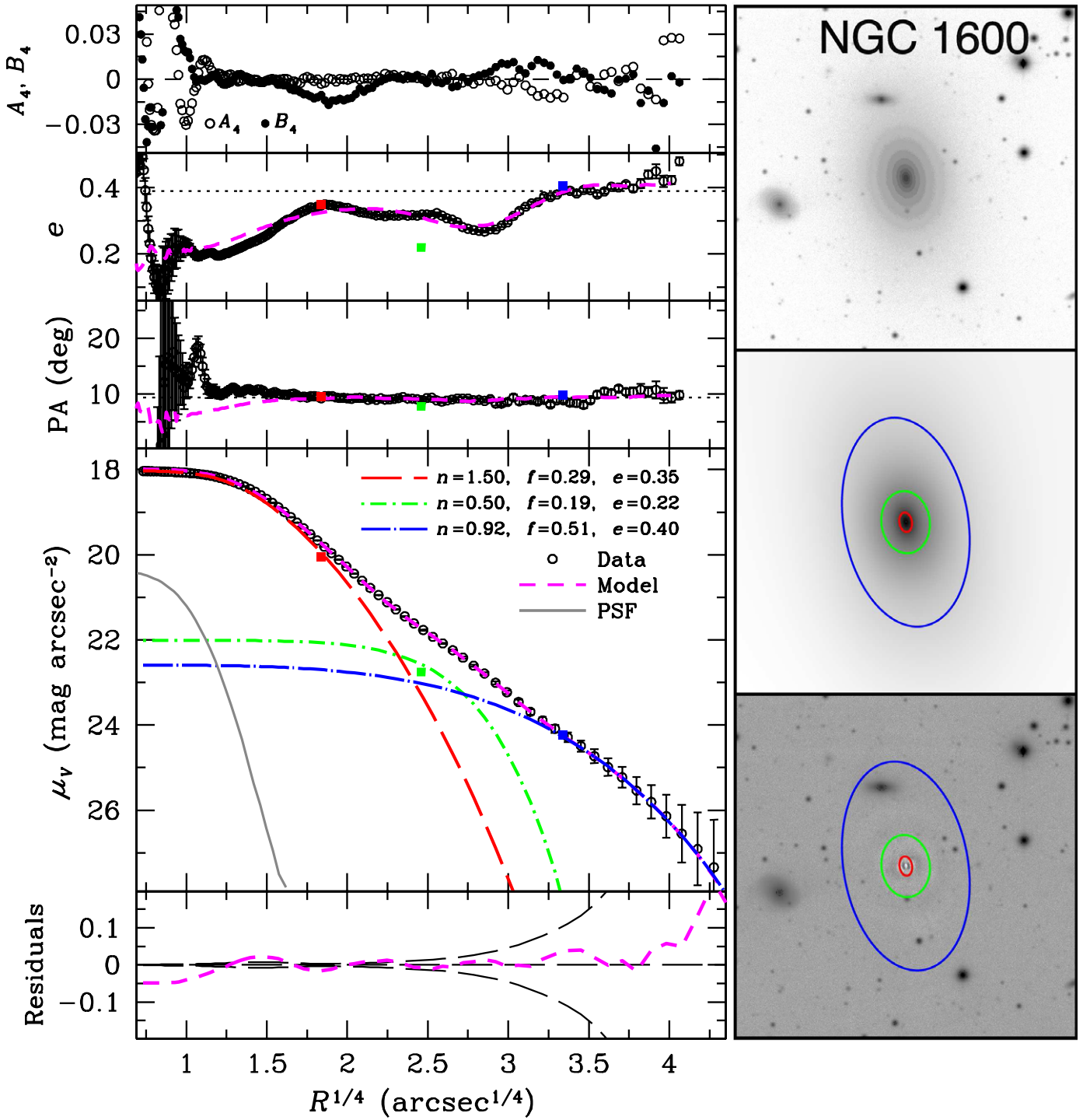
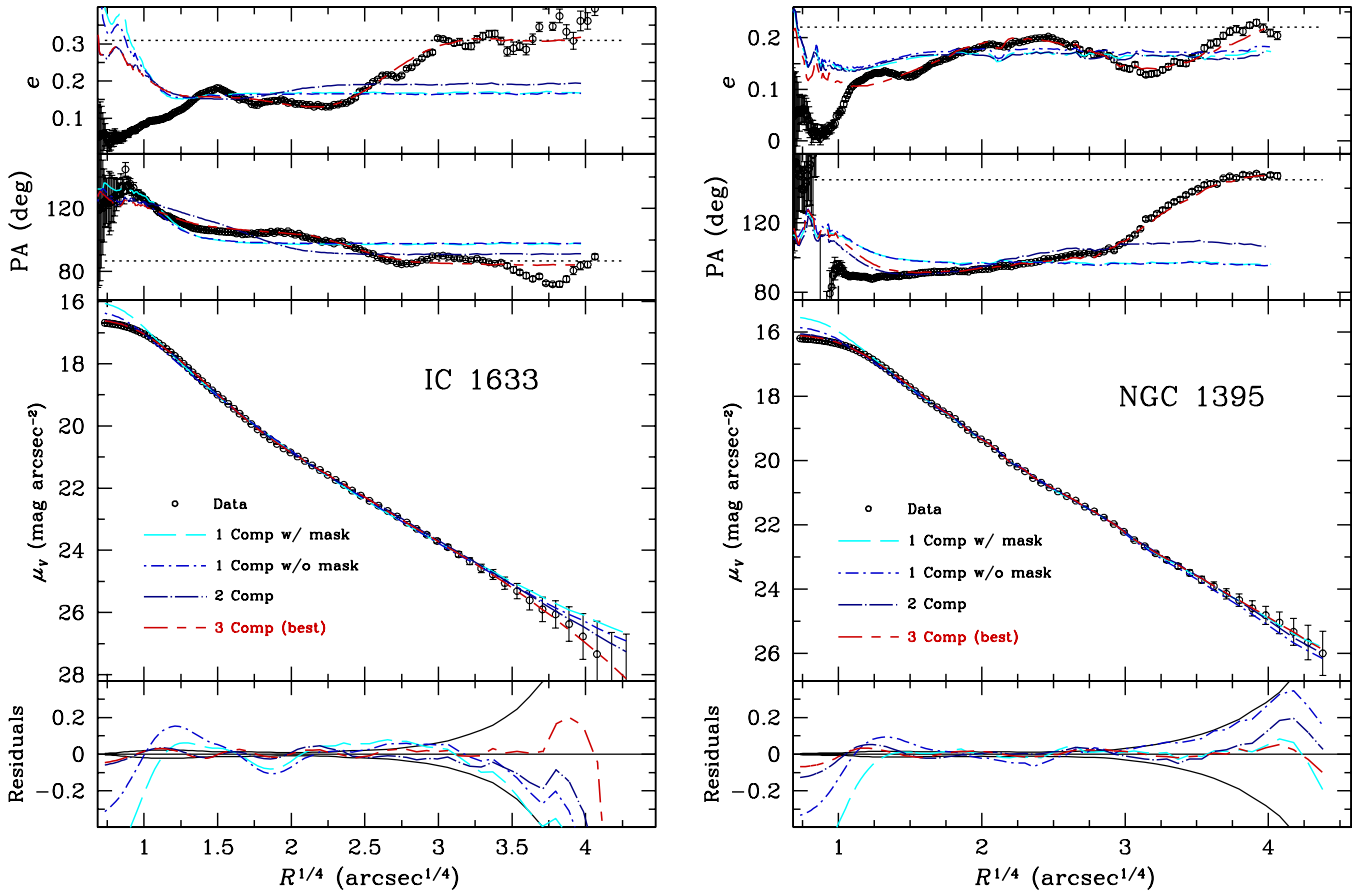


Figure 7. Best-fit three-component model for NGC 1600. See Figure 5 for details.

(A color version of this figure is available in the online journal.)

seamlessly with one another. Sometimes neither the 1D nor the 2D residuals offer much help to discriminate between models, because different models often produce only minor differences in the residuals. However, this ambiguity can be resolved if the subcomponents have different shapes, even if the differences are subtle. When evaluating the viability of different models, we find that the information furnished by the radial variation of ellipticity and PA provides very valuable constraints to decide which is the best solution. This is illustrated in Figure 8 for

IC 1663 and NGC 1395, where we compare the 1D information for different models. Even though the 1D residuals of the two- and three-component fits are quite similar, clearly only the three-component models can *simultaneously* follow the surface brightness, ellipticity, and PA profiles. This not only demonstrates the improvement provided by the three-component models but illustrates the distinct advantages of 2D image decomposition compared to traditional 1D profile fitting. Of course, one can always attempt to fit multiple components in 1D, and, in



**Figure 8.** Comparison of different models for IC 1633 and NGC 1395. We show a single-component Sérsic model, with and without a central mask, followed by a two-component model and the best-fitting three-component model. The single-component models clearly give inferior fits. While the models with both two and three components yield much improved residuals, only the three-component model can self-consistently match the  $\mu$ ,  $e$ , and PA profiles. It is clear that the three-component model does a superior job of recovering not only the  $\mu$  profile but also the geometric constraints provided by the  $e$  and PA profiles.

(A color version of this figure is available in the online journal.)

principle, one can perhaps even obtain better residuals. However, it will be very hard to prove the necessity of any extra component or to understand its nature. 2D analysis takes maximum advantage of the full information contained in a galaxy image. Any further, unnecessary compression of information should be avoided.

Interestingly, roughly 20% of the galaxies require even more complex models to explain their structure. The 18 galaxies with four-component models come in three flavors.

1. *Real substructures.* The most common category consists of galaxies that contain additional substructure such as a small edge-on disk (e.g., NGC 7029) or an outer ring (e.g., IC 2006). Figure 9 illustrates the case of NGC 7029, a galaxy classified as S0 by Sandage & Tammann (1981) but as E6 in the RC3. The 1D information in Figure 9 and the residual images in Figure 10 clearly demonstrate the impressive improvement made by the four-component model, which includes a moderately compact ( $R_e = 2.31$  kpc), edge-on ( $e \equiv 1 - q = 0.81$ ), disk-like structure described by a very low Sérsic index ( $n = 0.47$ ). Apart from the embedded disk, the global spheroidal structure of the rest of the galaxy resembles that typically seen for the bulk of the sample, namely consisting of an inner, middle, and outer component. NGC 7029, having a structure intermediate between an idealized elliptical and S0, illustrates the ambiguity that can arise. From the standpoint of the four-component structure, the galaxy may be regarded as an extreme case of an

S0 with a small disk ( $f = 0.02$ ) and a large spheroid. At the same time, it can be viewed as an elliptical with an embedded disk, perhaps acquired from a recent merger event. Either way, this example showcases the power of our 2D, multi-component decomposition technique. The disk component in NGC 7029 is so subtle and inconspicuous that it would be very difficult, if not impossible, to isolate it with any other method.

2. *Inner complications due to dust or unresolved structures.* Another class of four-component models describes systems that require a minor component to account for central dust structures or other nuclear features. This does not necessarily mean that all four components are physically separate and meaningful. For example, a dust lane present in the central region could induce a “break” in the inner luminosity distribution. Without taking this effect into account, the model could produce an unreasonable component with extremely high Sérsic index. Sometimes introducing another small component can greatly help alleviate such an effect, even if such a component is not a physically separate entity. Figure 11 shows the case of NGC 7507, an almost perfectly face-on elliptical that is considered a prototypical E0 galaxy. The structure of this galaxy, including the mild change of PA, is very well reproduced by a four-component fit. Apart from an extra, very small component in the inner region, the rest of the galaxy is well fit by a standard three-component structure. The size of this small

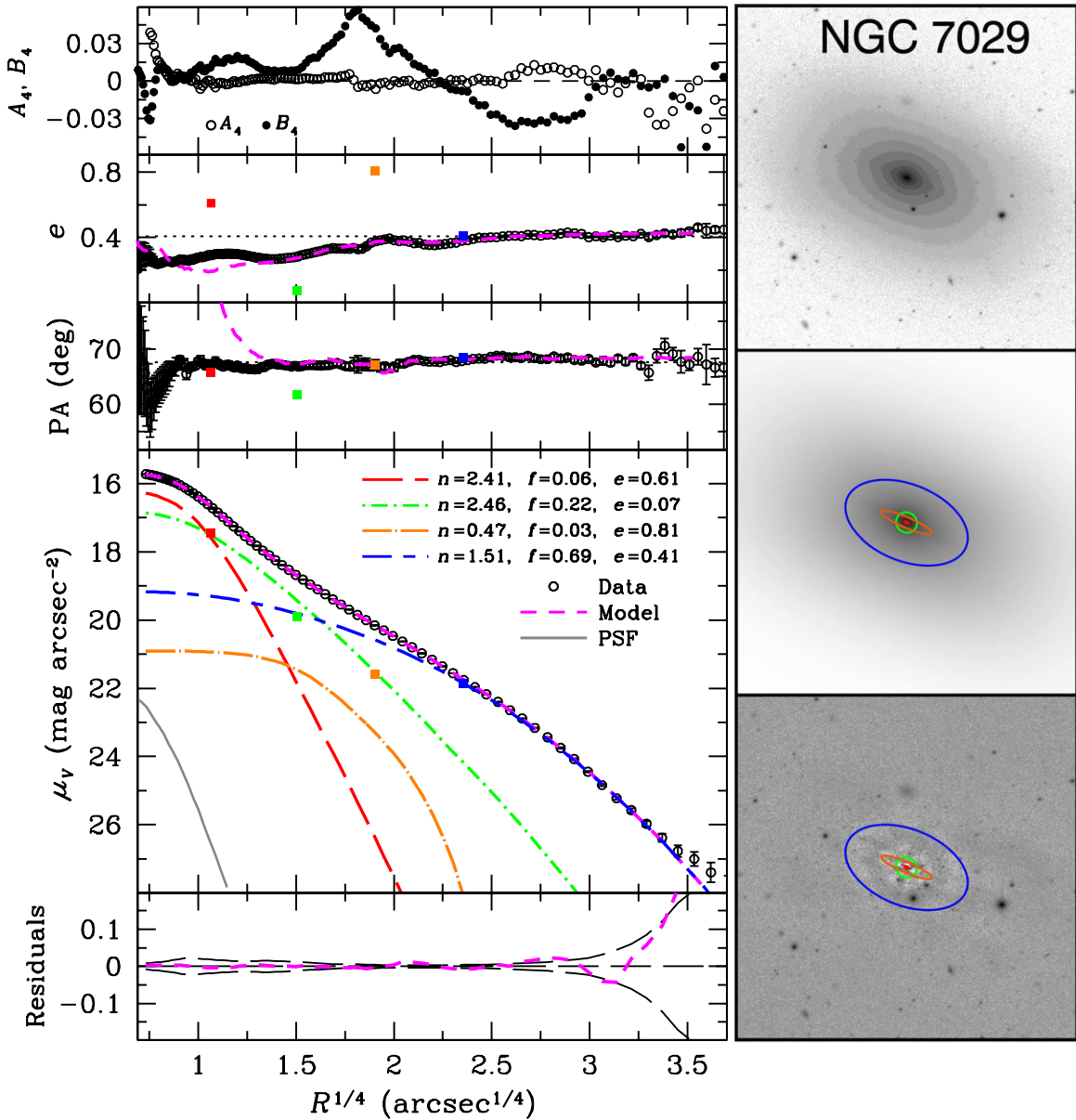


**Figure 9.** Best-fit four-component model for NGC 7029. See Figure 5 for details. The best fit requires a component (shown in orange dot-long dashed line) with high ellipticity. The radial profiles of surface brightness and geometric parameters do not provide strong constraints for the high-ellipticity component because it contains only a small fraction (3%) of the total light, but, as illustrated further in Figure 10, it can be clearly seen in the 2D analysis. This highlights the importance of the 2D approach.

(A color version of this figure is available in the online journal.)

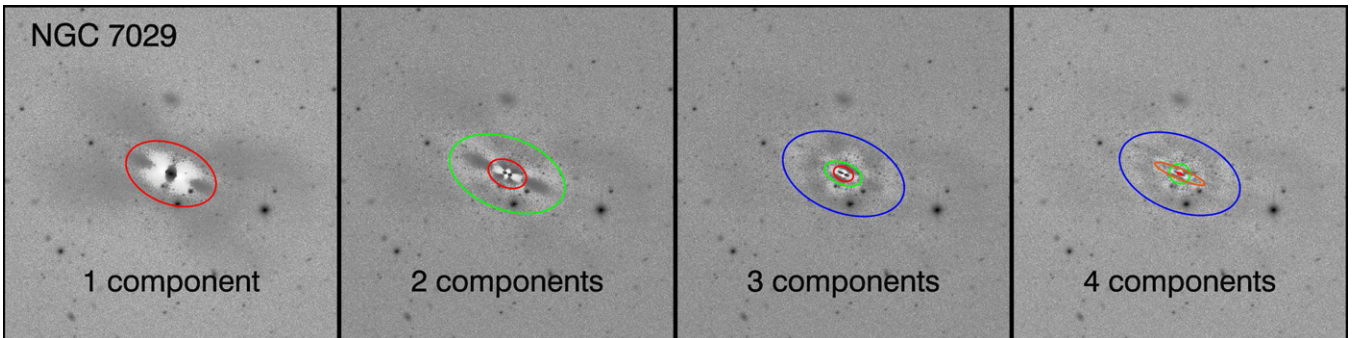


**Figure 10.** Comparison of residual images from different models for NGC 7029. Only the four-component model correctly reproduces the inner, high-ellipticity structure.

(A color version of this figure is available in the online journal.)

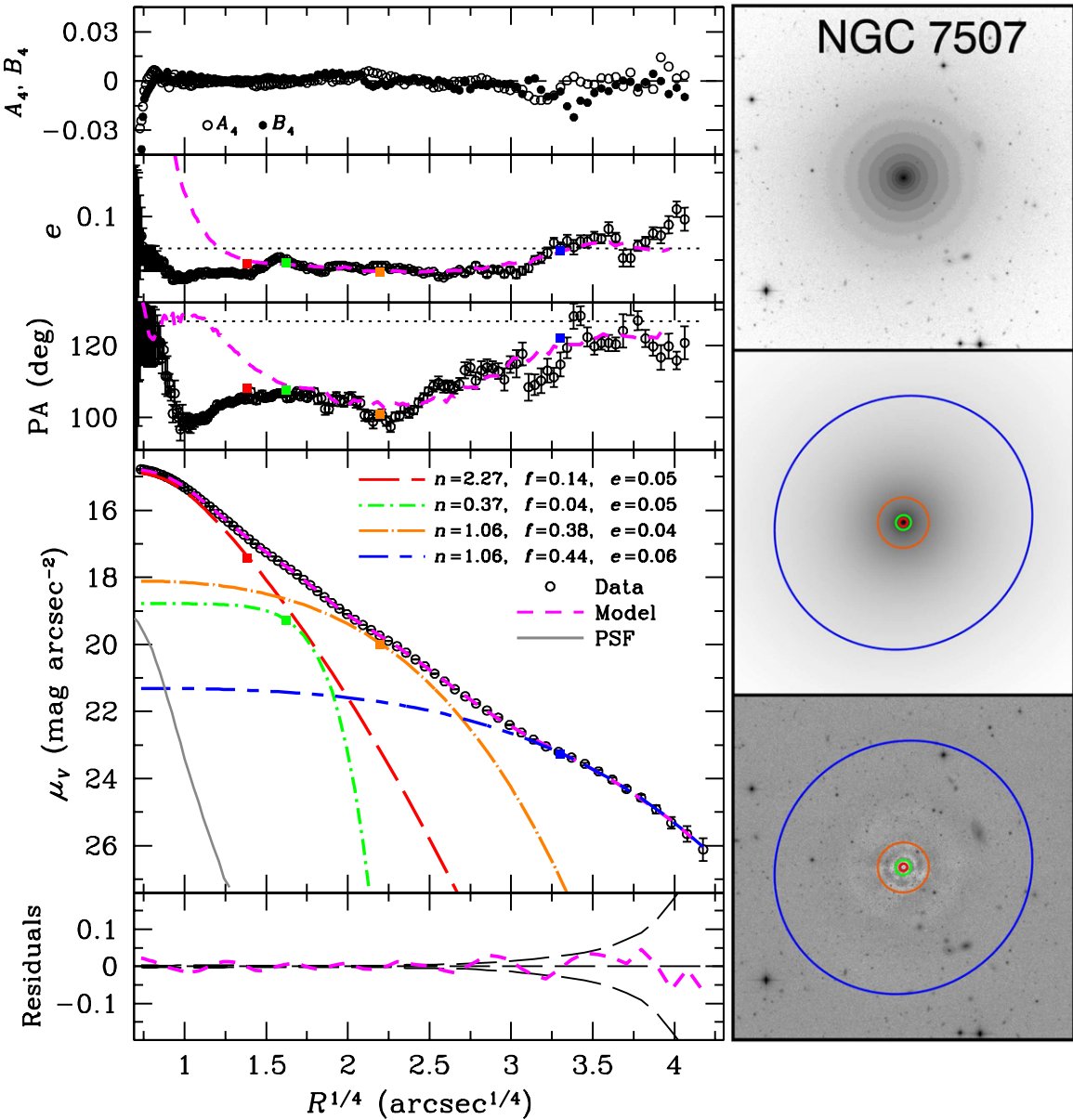


**Figure 11.** Best-fit four-component model for NGC 7507. See Figure 5 for details. The geometric information is less useful to constrain the fit in this case because of the low inclination angle of the galaxy. This model includes a very small component (4% of total luminosity; green dot-short dashed line), which does not have an obvious physical explanation, but is necessary to produce a good model, as illustrated further in Figure 12.

(A color version of this figure is available in the online journal.)

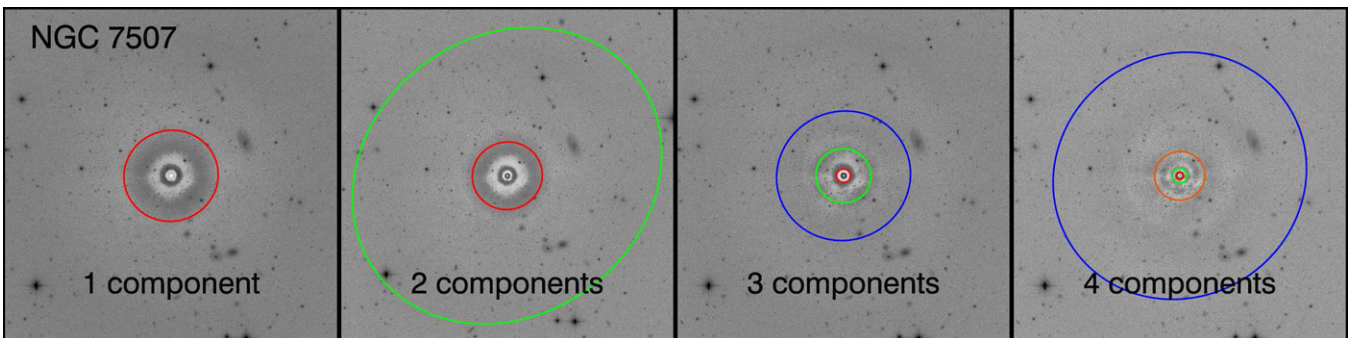


**Figure 12.** Comparison of residual images from different models for NGC 7507. The four-component model clearly gives the best fit.

(A color version of this figure is available in the online journal.)

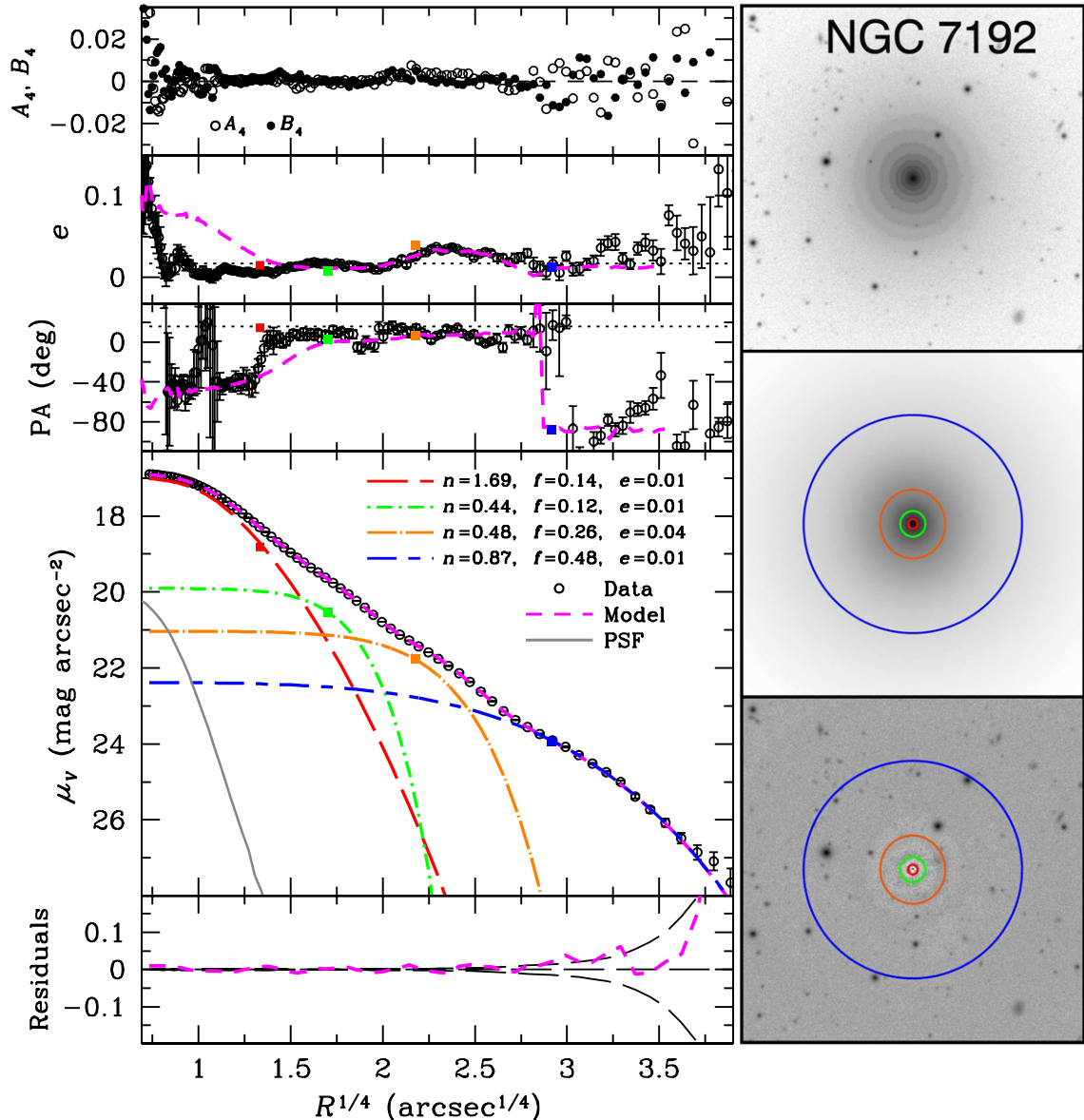


**Figure 13.** Best-fit four-component model for NGC 7192. See Figure 5 for details. Although it is also a face-on system, the near-exponential ( $n = 0.87 \simeq 1$ ) extended component is consistent with it being a disk, and thus this galaxy may be a misclassified S0. Additional models are shown in Figure 14.

(A color version of this figure is available in the online journal.)

component ( $R_e = 0.75$  kpc) is very similar to the component that dominates the inner region ( $R_e = 0.4$  kpc), and its Sérsic index is quite low ( $n = 0.37$ ). Although this component has a very low luminosity fraction ( $f = 0.04$ ), it is essential for constructing a reasonably good model for this galaxy. By comparing the residual images of models with different numbers of components (Figure 12), it is easy to see that the four-component model fares the best. As for the nature of this small component, it should be viewed as part of the inner structure since it is likely to be associated with the “extended region of dust absorption on the southwest side of the nucleus” (Goudfrooij et al. 1994).

3. *Misclassified S0s.* The third category of galaxies that requires an extra fourth component to achieve a satisfactory fit comprises misclassified S0s. For these galaxies, the evidence for their S0 nature comes from either the existence of a bar-like structure in the residual image of the two- or three-component model (e.g., NGC 584) or the presence of

disk-like properties in the outermost component, as in the case of NGC 7192 (Figures 13 and 14). This almost face-on galaxy is classified as a cD galaxy in the RC3 on account of the contrast between the inner region and the outer extended feature, but it was classified as an S0 in the Carnegie Atlas of Galaxies (Sandage & Bedke 1994). Our four-component model recognizes this galaxy as an S0 from its multiple “lens” structures. The innermost bulge component has the highest Sérsic index ( $n = 1.7$ ) and accounts for about 14% of the total luminosity. The disk, comprising 48% of the total luminosity, is the outermost component with  $n \approx 0.9$ . The “lens” structures are the two intermediate-scale components with Sérsic indices  $n \approx 0.4\text{--}0.5$ , which altogether account for 38% of the total light. Our four-component model is qualitatively similar to the  $K$ -band decomposition presented by Laurikainen et al. (2010), although the detailed parameters of the subcomponents are different. Unlike Laurikainen et al., we do not restrict the

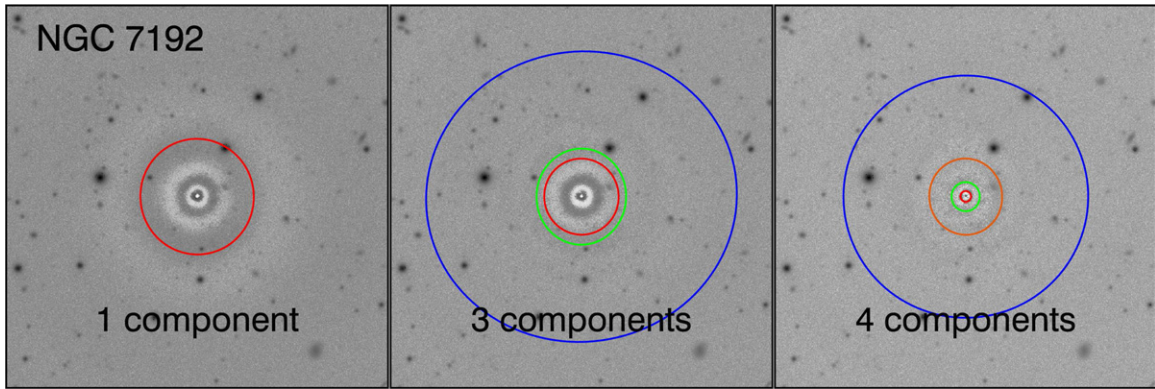


**Figure 14.** Comparison of residual images from different models for NGC 7192. From left to right, residual images are shown for models with one, three, and four Sérsic components; the two-component model is unreasonable and is excluded. The four-component model clearly gives the best fit.

(A color version of this figure is available in the online journal.)

model parameters to fixed values (e.g., setting  $n = 1$  for an exponential disk).

Apart from the misclassified S0s, the additional component invoked for the other two types of four-component fits comprises only an insignificant fraction of the light ( $\leq 5\%$ ). Nevertheless, it can be extremely helpful in terms of improving the global model of the galaxy. Setting aside this extra perturbation, the other main components have properties similar to, and can be easily identified with, the standard three components that normally suffice to describe the overall structure of the sample. In other words, these more complicated four-component models do not violate our main thesis: that nearby ellipticals contain three main structural components.

#### 3.4. Definition of a “Good” Model

There is no unique or rigorous definition of a “good” model in image decomposition. Whether a fit is “good” or “good enough” depends on the fitting method as well as on the scientific application. In 1D fitting, the residual profile is often used to judge the quality of the fit. Yet, we know that the 1D method cannot fully take into account geometric constraints, and sometimes it cannot resolve the degeneracy between different components. Both of these limitations are especially problematic for elliptical galaxies, which tend to show only mild or gradual changes in surface brightness and geometric parameters. As a case in point, K09 successfully fit a single Sérsic function to the 1D global surface brightness distribution of the giant elliptical galaxy M87 (NGC 4486; see their Figure 10) after judiciously choosing a radial range that excludes the inner and outer portions of the profile. From the standpoint of the residual profile, their fit is perfectly acceptable within the specified radial range used in the fit. However, does this mean that this is the correct model for M87? Two clues suggest otherwise. First, as can be seen from Figure 10 of K09, the ellipticity of the outer regions of M87 is significantly higher than that of its inner region; the PA varies with radius too, albeit less drastically. Although the radial variation of  $e$  and PA can conceivably be explained by isophotal twisting of a single component, an alternative (and according to the results of this paper, more likely) interpretation is that it is a manifestation of the superposition of more than one physical component. Second, the single-component fit yields a very high Sérsic index of 11.8. Although there is no strong physical justification to restrict the Sérsic index below any particular value, such a high index may be driven by the fact that M87 has an extended envelope.

For 2D image decomposition, the quality of the model is judged usually in one of three ways. The most direct one is to examine the residual image, after appropriate scaling and enhancement. This method is straightforward and efficiently identifies obvious problems with the fit, since a “bad” model often leaves strong residual features. However, when degeneracy between components exists in the model, or when two models only differ at a moderate level, the residual image alone does not offer enough discrimination. Another common approach uses empirical parameters to quantify the goodness of fit. The general idea is to compare the relative absolute flux left in the residuals, either to the photometric uncertainties or to the luminosity of the galaxy inside a certain aperture. This method can efficiently weed out problematic models for a large sample, or it can be used to compare the average quality of different models within a given sample. However, since it uses integrated information, it is not effective at diagnosing the details of the model or for comparing various models when the differences are subtle. Lastly, it is common to extract the 1D surface brightness profile from a 2D model and compare it with that derived from the original data. This method is not as intuitive as inspecting the residual image directly, but it is relatively sensitive to mild differences between models, as shown in Figure 8.

Different scientific applications set different standards and require different strategies for model comparison. While single-component 2D fitting can efficiently extract global parameters for large samples of distant galaxies (e.g., Hoyos et al. 2011), whose resolution and image depth often do not warrant more complex structural analysis, here we are facing the opposite regime. Our sample is specifically designed to yield maximum information on the internal structure of nearby, bright galaxies, and we must strive for a higher standard of model acceptability and devise a more comprehensive strategy for model comparison. For our purposes, we define the “best” model as one that contains a *minimum number of components with reasonable, robust parameters that describes visibly distinct structure*. Here the word “visibly distinct” has two layers of meaning. First, both the surface brightness distribution and the systematic radial change of geometric information should be recovered down to a certain level, which means that the level of the residuals should be consistent with the stochastic rms error. Second, the amount of information that can be recovered is also directly related to the data quality (e.g., spatial resolution, seeing, signal-to-noise ratio). Therefore, a selected “best” model should only be considered as the model that recovers “enough” photometric

information on a certain image. While we do not visually identify components by eye, we should mention here that often the individual components correspond to noticeable breaks in the surface brightness profile or distinct features on 2D images.

Increasing the number of components adds more degrees of freedom. It is always possible to reduce the residuals or  $\chi^2$  by making the model more complex. This is dangerous and can lead to overinterpretation of the data. As previously stated, our approach errs on the side of caution: We restrict our models to the fewest components possible and slowly increase in complexity only as absolutely justified by the data. We further demand that the fitted components have “reasonable” parameters, ones that are well constrained by prior empirical knowledge or by the data themselves. For example, Sérsic indices with extremely high (e.g.,  $n \gtrsim 10$ ) or low (e.g.,  $n \lesssim 0.1$ ) values should be regarded with suspicion, and effective radii larger than the size of the image are untrustworthy. If the fit returns a component with high ellipticity, a flattened structure should be directly identifiable on the image or in the residuals. In all cases, the model parameters should be robust with respect to potential systematic errors introduced by the seeing or the sky background. In short, while there is no fully objective or completely automatable procedure to select the best-fit model, we exercise due diligence and uniform methodology that is based on reasonable expectations for the structure of galaxy subcomponents to examine the models case-by-case, using *all* the constraints furnished by the data, both in their 1D and 2D representation.

### 3.5. Model Selection and Sample Statistics

To quantify the relative goodness of fit for the various models and to compare them in a statistical manner, we compute the integrated absolute value of the 1D residuals inside  $V$ -band  $R_{50}$  and  $R_{80}$ , the radii enclosing 50% and 80% of the total light (Paper I). Figure 15 shows that the residuals decrease markedly in going from single- to multiple-component models. The improvement from two to three components is less dramatic, but it is clear that three components give systematically smaller residuals than two components, and that the tail of high-residual objects disappears. These trends are present for the integrated residuals within both  $R_{50}$  and  $R_{80}$ . Following Hoyos et al. (2011), we also define the excess variance index,

$$\text{EVI} = \frac{1}{3} \left( \frac{\sigma_{\text{res}}^2}{\langle \sigma_{\text{img}}^2 \rangle} - 1 \right), \quad (2)$$

where  $\sigma_{\text{res}}$  is the root mean square of the residuals within  $R_{80}$  (Hoyos et al. use a somewhat different aperture, but this difference is immaterial) and  $\sigma_{\text{img}}$  is the root mean square of the Poisson noise in the same area. In a perfect model, excess variation index (EVI) = 0.0; if EVI  $\gg 1$ , the model deviates significantly from the actual data. Figure 16 shows that, as expected, EVI generally correlates with the integrated 1D residuals. According to Hoyos et al. (2011), EVI  $> 0.95$  is probably indicative of an inadequate model. We cannot strictly apply the same numerical criterion to CGS, whose data are very different from those considered by Hoyos et al., but we can easily see that EVI decreases dramatically as the number of components increases from one to three. Impressively, most galaxies that require a three-component fit have EVI  $< 1$ ; by contrast, most of the single-component fits return EVI  $\gg 1$ . In no instance is a single-component fit ever superior to a more complex model according to the EVI. This may sound like a

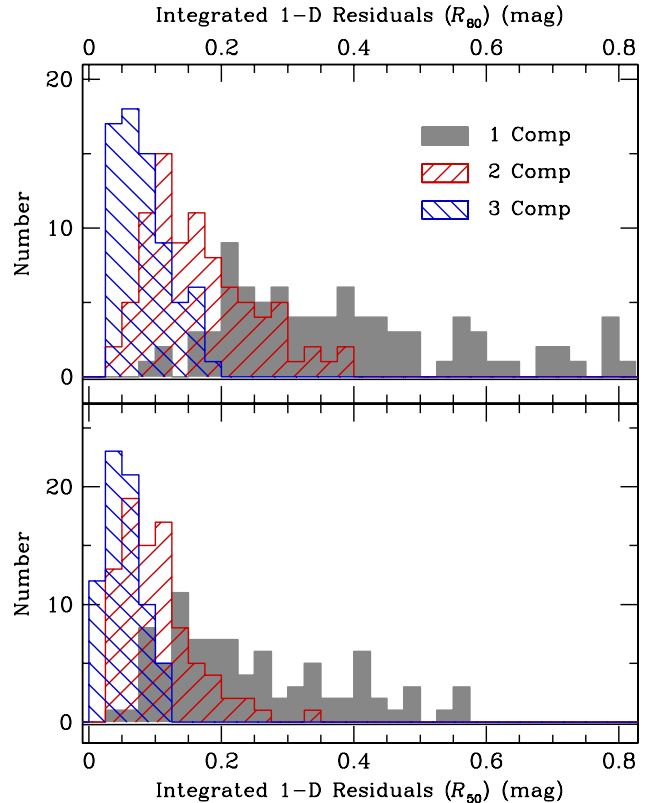


**Figure 15.** Distribution of integrated 1D residuals within (top)  $R_{80}$  and (bottom)  $R_{50}$ . These parameters are used to diagnose the goodness of fit of models with different number of components. The models include one (without central mask), two, and three Sérsic components.  
(A color version of this figure is available in the online journal.)

trivial statement since the inclusion of more components adds more degrees of freedom to the fit, hence will result in lower residual level. But we remind the reader that our standard for the “best” model and the method to select such a model rely only partly on the residual level. We require the best model to be one that recovers as much information as possible using the minimum number of components. Therefore, the above statement should be understood as “no single-component model provides enough information to recover the 2D luminosity distribution of ellipticals in this sample.” Even without further analysis, we can conclude from this that nearby ellipticals almost always have global structures more complicated than can be described by a single Sérsic function. The majority require multiple photometric components.

Among the sample of 94 CGS ellipticals, 70 can be robustly fit with a three-component Sérsic model.<sup>12</sup> And, using different types of tests, including ones with dramatically different initial parameters, these models also prove to be quite stable. Five galaxies (IC 4742, NGC 1404, 1453, 5018, 5077) were modeled with two components, but their fits suffered from a variety of complications (e.g., nearby bright objects, central dust features, strong tidal features, etc.) that preclude us from obtaining a more refined model. The remaining 18 galaxies require four

<sup>12</sup> A possible edge-on structure is present in NGC 3585, but it is very subtle and difficult to isolate; since the standard three-component model already yields a reasonable fit with low residuals, we decided not to pursue a more complicated fit. The merger remnants NGC 1700 and NGC 2865 can be fit with more complex models to account for their irregular, low-surface brightness tidal features, but we prefer to be conservative and restrict the final models to the standard three components.

**Table 2**  
Statistical Properties of the Subcomponents

Parameter	Inner			Middle			Outer		
	Mean	SD	Median	Mean	SD	Median	Mean	SD	Median
$R_e$ (All) (kpc)	0.80	0.51	0.64	3.18	2.25	2.50	14.10	10.28	10.46
$R_e$ ( $M_V \leq -21.3$ mag)	0.90	0.61	0.74	4.17	2.57	3.47	20.03	10.75	17.76
$R_e$ ( $M_V > -21.3$ mag)	0.70	0.35	0.64	2.04	0.90	1.90	7.43	2.58	6.60
$\mu_e$ (All) (mag arcsec $^{-2}$ )	19.32	0.91	19.28	21.30	0.95	21.24	23.39	0.85	23.20
$\mu_e$ ( $M_V \leq -21.3$ mag)	19.20	0.73	19.18	21.28	1.05	21.23	23.64	0.87	23.79
$\mu_e$ ( $M_V > -21.3$ mag)	19.46	1.05	19.42	21.34	0.82	21.32	23.10	0.71	23.07
$M_V$ (All) (mag)	-19.25	1.05	-19.33	-19.87	1.24	-19.78	-21.05	0.87	-21.06
$M_V$ ( $M_V \leq -21.3$ mag)	-19.46	1.09	-19.68	-20.67	0.92	-20.88	-21.69	0.62	-21.68
$M_V$ ( $M_V > -21.3$ mag)	-19.01	0.94	-19.10	-18.99	0.87	-19.20	-20.36	0.49	-20.34
$n$ (All)	2.47	1.95	1.98	1.52	1.12	1.24	1.63	0.67	1.56
$n$ ( $M_V \leq -21.3$ mag)	1.74	1.52	1.49	1.72	1.15	1.63	1.67	0.77	1.63
$n$ ( $M_V > -21.3$ mag)	3.24	2.05	2.60	1.30	1.01	0.92	1.58	0.50	0.71
$e$ (All)	0.24	0.12	0.25	0.26	0.16	0.24	0.28	0.14	0.28
$e$ ( $M_V \leq -21.3$ mag)	0.22	0.14	0.21	0.23	0.14	0.20	0.29	0.13	0.27
$e$ ( $M_V > -21.3$ mag)	0.24	0.09	0.26	0.30	0.19	0.27	0.26	0.14	0.29
$f$ (All)	0.16	0.11	0.13	0.25	0.17	0.20	0.60	0.17	0.61
$f$ ( $M_V \leq -21.3$ mag)	0.10	0.08	0.08	0.29	0.19	0.21	0.61	0.19	0.55
$f$ ( $M_V > -21.3$ mag)	0.20	0.13	0.19	0.20	0.12	0.20	0.59	0.15	0.63

**Notes.** The mean, standard deviation (SD), and median value of several key parameters for the subcomponents of the three-component models. The components are designated inner, middle, and outer according to their relative effective radius.

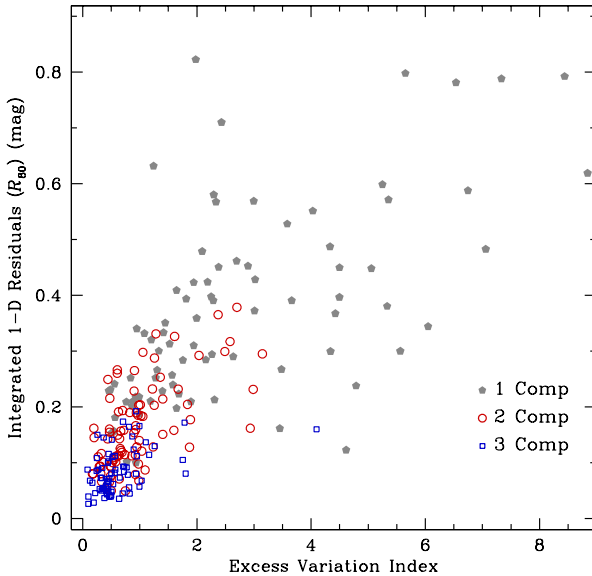


**Figure 16.** Relation between the integrated 1D residuals within  $R_{80}$  and the excess variation index (EVI) defined by Equation (2), another parameter that indicates the goodness of fit of the models. The models include one (without central mask), two, and three Sérsic components.

(A color version of this figure is available in the online journal.)

components. Among these, three (ESO 221-G026, IC 2006, NGC 7029) need a fourth component to account for minor structures such as an edge-on disk or an outer ring; seven (IC 2311, NGC 3078, 4786, 5796, 6876, 7145, 7196, 7507) contain an extra central, compact component of an unspecified nature, but most likely attributable to unresolved nuclear dust features; eight (IC 4797, NGC 584, 3904, 4033, 4697, 6673, 7144, 7192) we deem to be misclassified S0s.

The final decompositions for the sample are presented in Appendix E, where we show an atlas designed to help visualize the 1D and 2D information of each best-fit model. Table 1 lists

the parameters for the final models. Table 2 summarizes the statistical properties of the parameters for the subcomponents of the 70 galaxies fitted with a three-component model.

### 3.6. Uncertainties

It is nontrivial to calculate errors for the parameters of our multi-component fits. Lessons learned in the context of single-component fitting of galaxy images (e.g., Guo et al. 2009; Yoon et al. 2011) do not easily translate to our case. Because our galaxies are very bright and highly resolved, the error budget is limited neither by signal-to-noise ratio nor by the PSF, which affects only the very central region. Instead, the dominant source of uncertainty comes from errors in sky background level estimation. We approach this problem empirically, by manually adjusting the sky pedestal within the range of values constrained by our sky measurement procedure (Section 3.1 and Appendix B) and systematically re-running the fits. For a given parameter, the largest absolute variation normalized to the average value from the different outputs (e.g.,  $|\Delta R_e|/R_e$ ) gives its relative uncertainty. On average, the relative uncertainties are quite small. The parameters most vulnerable to sky uncertainty are the effective radius and the Sérsic index. For the inner component, the mean uncertainty for  $R_e$  is  $\sim 8\%$  and for  $n \sim 17\%$ . They get worse for the other two components, increasing to 18% and 35%, respectively, for the middle component and 25% and 39% for the outer component. These uncertainties apply to galaxies for which  $R_{\text{img}}/R_{50} \gtrsim 5$ ; they can be significantly larger for more extended sources. Notwithstanding these complications, the main result of this paper—that most nearby elliptical galaxies have a three-component structure—is robust.

## 4. RESULTS

The central result that emerges from this work is that the global photometric structure of nearby elliptical galaxies can be

described most generally by three Sérsic components. Ranking them by physical size, we designate them the inner, middle, and outer components. This is not the first time that multiple components are used to model nearby ellipticals. For example, in a recent paper, Dhar & Williams (2012) interpret the 1D surface brightness profiles of ellipticals from K09 using a linear combination of two or three components. However, as we emphasize in this paper, it is important to take into account the full 2D information in the photometric decomposition. This section (see also Table 2) summarizes the statistical properties of key parameters for these subcomponents and demonstrates that they follow well-behaved photometric scaling relations. To put these results in context with the literature, we also compare them with results from more traditional single-component fits. As many properties of ellipticals are known to depend systematically on luminosity or stellar mass, we discuss the sample collectively as well as separately for a high-luminosity and a low-luminosity subsample, where the division between the two is taken to be  $M_V = -21.3$  mag, the median  $V$ -band total luminosity. In a companion paper, we explore the implications of these results for the current paradigm of elliptical galaxy formation.

#### 4.1. Distribution of Key Parameters

The size and size ratios of the substructures offer useful insights into the size evolution of ellipticals, currently a topic of much research (e.g., Naab et al. 2009; van Dokkum et al. 2010). Figure 17 shows the distribution of effective radii. For a traditional single-component Sérsic fit, the median  $R_e$  is 5.8 kpc; this value is insensitive to whether the fit is done with or without a central mask. Applying our new fitting methodology, the three subcomponents become well separated in size, having median  $R_e = 0.6, 2.5$ , and  $10.5$  kpc for the inner, middle, and outer components, respectively. On average, high-luminosity ellipticals have larger effective radii for all three components. The outer component of the high-luminosity sample has a typical  $R_e \approx 17.8$  kpc, 5 times larger than the middle component ( $R_e = 3.5$  kpc); by contrast, in the low-luminosity group the outer component is only 3 times as large as the middle component ( $\sim 6.6$  versus 1.9 kpc).

In both groups the inner component is a compact, sub-kiloparsec structure. It has relatively low luminosity ( $M_V \approx -19.3$  mag; Figure 18) and accounts for only 8%–20% of the light (Figure 19). Most of the light resides in the middle and outer components, with the latter responsible for  $\sim 60\%$  of the light in both luminosity groups and the former for  $\sim 20\%$ . Thus, the outer, most extended component dominates the luminosity—and presumably the mass—of nearby ellipticals.

One of the most unexpected outcomes from our analysis is that the ellipticity of the isophotes systematically increases toward large radii. This is a robust, model-independent result, which can be seen even from a straightforward comparison of the 1D ellipticity profile at  $R_{20}$  and  $R_{80}$ . Figure 20 shows that  $e_{R80} - e_{R20}$  is skewed slightly ( $\Delta e < 0.1$ ), but definitely, toward positive values: The outer regions are generally more flattened than the inner regions. This phenomenon is shown more explicitly in Figure 21 for the 70 ellipticals decomposed with three components. As before, the outer component is, on average, more flattened than either the inner or middle components. When the sample is separated into the two luminosity bins, we see that the effect occurs almost exclusively within the high-luminosity subsample (panel b), not in the low-luminosity objects (panel c). The ellipticity distribution of the total sam-

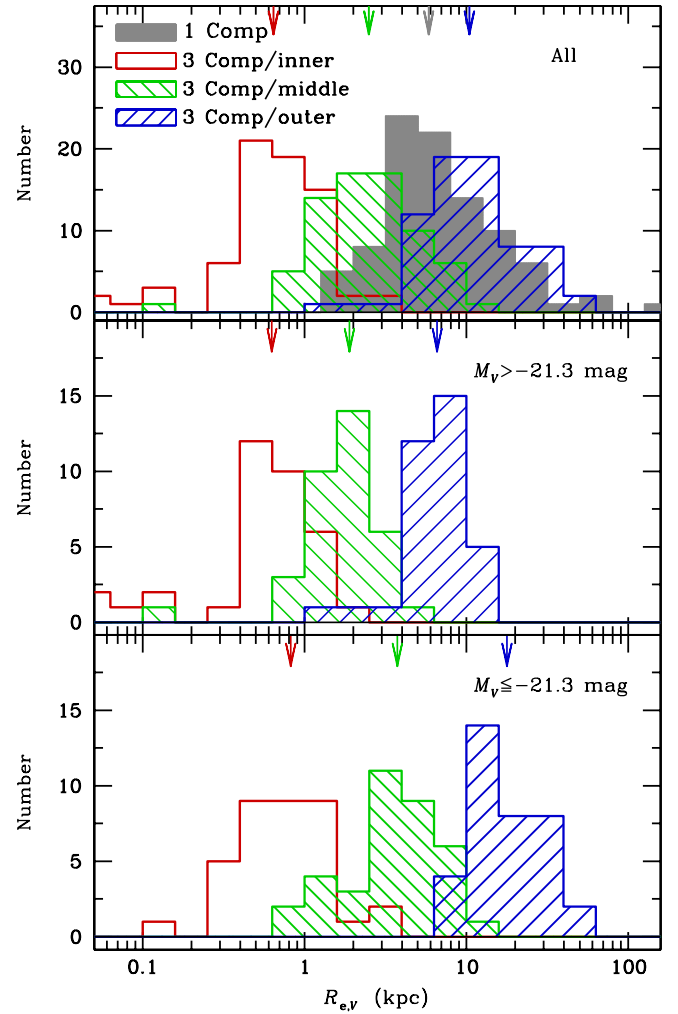


**Figure 17.** Distribution of effective radius in the  $V$  band. The top panel compares the individual subcomponents of the three-component model with the single-component model. The middle and bottom panels separate the sample into the low-luminosity and high-luminosity groups, respectively, defined to be those above and below the median value of  $M_V = -21.3$  mag. The median values of  $R_{e,V}$  for the various components are indicated by the arrows.

(A color version of this figure is available in the online journal.)

ple exhibits another interesting feature: The middle component contains a high- $e$  tail. Closer inspection reveals that most of these highly flattened substructures reside in the low-luminosity sample, and they can be traced to small-scale, sometimes dusty disk-like structures embedded within the main body of the galaxy.

Ever since the seminal work of Caon et al. (1993), elliptical galaxies have been increasingly modeled using the Sérsic function. Apart from some investigations of brightest cluster galaxies (e.g., González et al. 2005; Donzelli et al. 2011), most studies describe the surface brightness distribution of the main body of ellipticals (after excluding the innermost and outermost regions; e.g., K09) using a single Sérsic index. For relatively luminous ellipticals, the resulting Sérsic indices are large, typically  $n \approx 3\text{--}6$ , but occasionally as high as 10 or even greater. Indeed, a high Sérsic index is often synonymous with early-type galaxies in general, and with ellipticals in particular. In this work, we demonstrate that the overall structure of ellipticals, in fact, is best described by not one, but three photometric subcomponents. It is thus not surprising that the Sérsic indices of the individual subcomponents turn out to

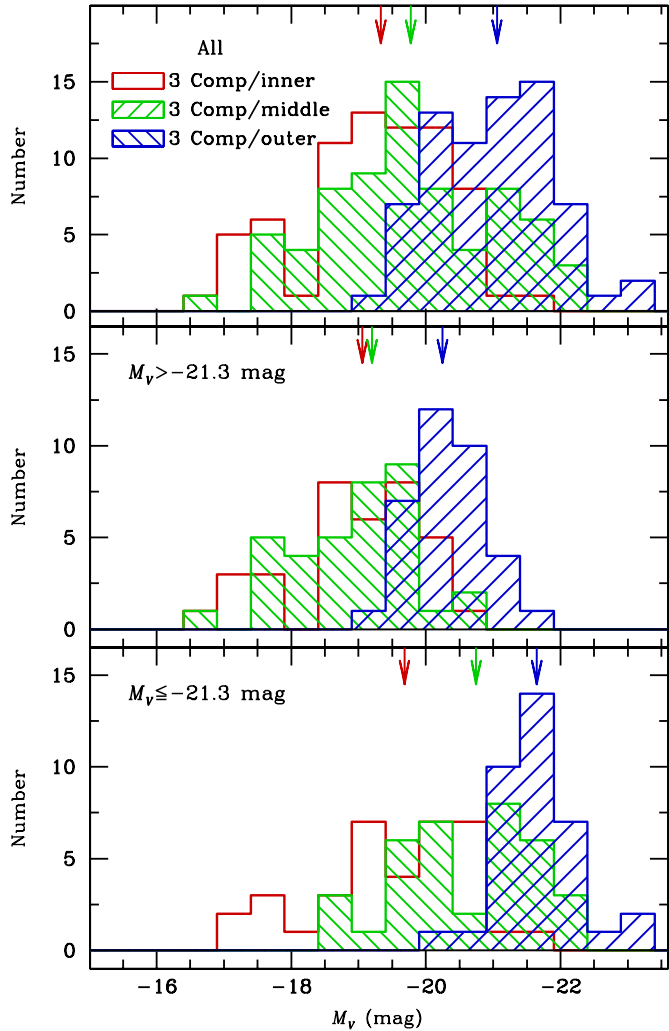


**Figure 18.** V-band absolute magnitude of the subcomponents for the three-component models, corrected for Galactic extinction. The three panels show the distribution for the entire sample and then separately for the low-luminosity and high-luminosity groups.

(A color version of this figure is available in the online journal.)

be substantially smaller than the values for the single-component fits (Figure 22). The inner, middle, and outer components all have rather similar Sérsic indices; their formal median values are  $n = 2.0, 1.2$ , and  $1.6$ , respectively. Very few fits yield  $n = 4$ . On the other hand, a sizable fraction of the components have  $n \lesssim 1$ . This is particularly noticeable for the middle component of the low-luminosity sample. In combination with the tendency for this component to appear flattened (Figure 21), it supports the notion that low-luminosity ellipticals contain embedded disks.

We further note that the Sérsic index of the inner component for the high-luminosity subsample ( $n = 1.5$ ) is significantly lower than that of the low-luminosity subsample ( $n = 2.6$ ). If we follow Lauer et al. (2007) and approximate the inner slope of the profile as a simple power law,  $\mu(R) \propto R^{-\gamma'}$ , the corresponding power-law index measured within the inner  $3''$  is  $\gamma' = -0.2$  for the high-luminosity sources and  $\gamma' = -0.6$  for the low-luminosity sources. This is remarkably close to the canonical values of the average inner slopes for “core” and “power-law” (or “extra-light”) ellipticals obtained from *HST* observations (e.g., Lauer et al. 2007). Although the resolution of the CGS images cannot compete with that of *HST*, it is reassuring to know that our detailed decomposition of the ground-

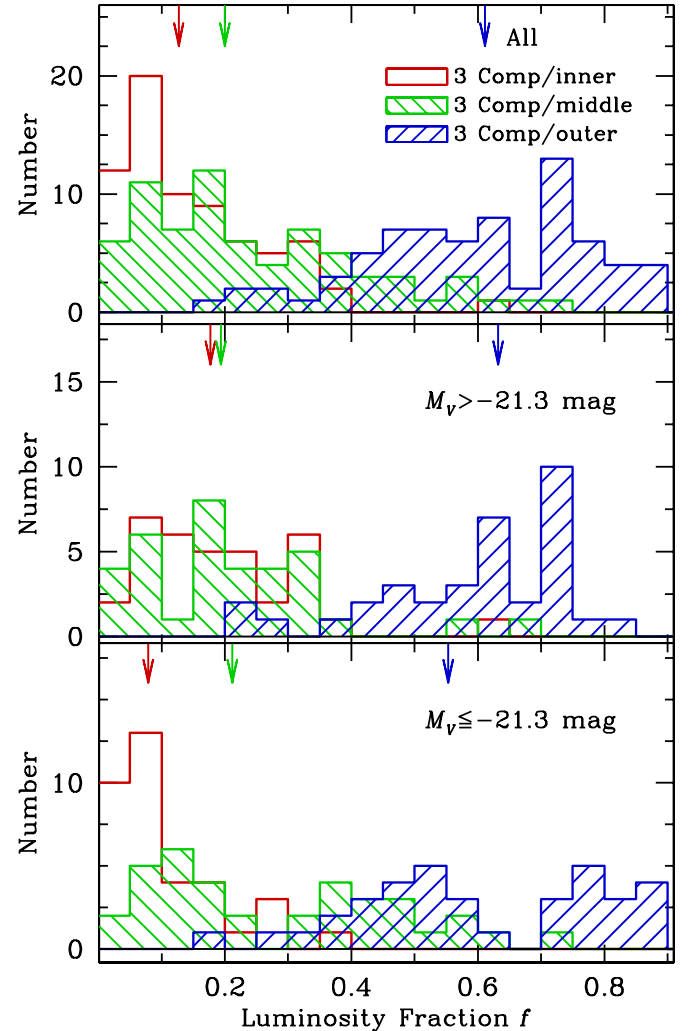


**Figure 19.** Luminosity fraction of the subcomponents for the three-component models. The three panels show the distribution for the entire sample and then separately for the low-luminosity and high-luminosity groups.

(A color version of this figure is available in the online journal.)

based data can essentially recover the gross properties of the nuclear regions.

Sky background errors greatly affect the Sérsic index. Given the complications involved in our sky determination (Section 3.1 and Appendix A), we are wary of overinterpreting the results on the Sérsic indices. To test the robustness of our conclusions, we re-examined the statistics for the subset of 48 objects with image sizes larger than  $6 \times R_{50}$ , for which we have very high confidence in their sky estimates. Reassuringly, none of the main conclusions change qualitatively.

Lastly, we look at the output from the Fourier analysis. Apart from some applications limited to quasar host galaxies (e.g., Kim et al. 2008), to our knowledge the Fourier mode capability of GALFIT 3.0 has yet to be applied extensively to study galaxy structure. On the one hand, it is reassuring that the Fourier modes do not strongly affect the results of our final models; on the other hand, we also find that the Fourier modes of each component are affected by different sources of uncertainties. For example, even after improving the object masks, nearby saturated stars and small galaxies can still greatly affect the amplitude of the Fourier modes. Dust features are also problematic. Given this complexity, we first restrict our attention to the  $m = 1$  mode. As the lowest order mode, it should be

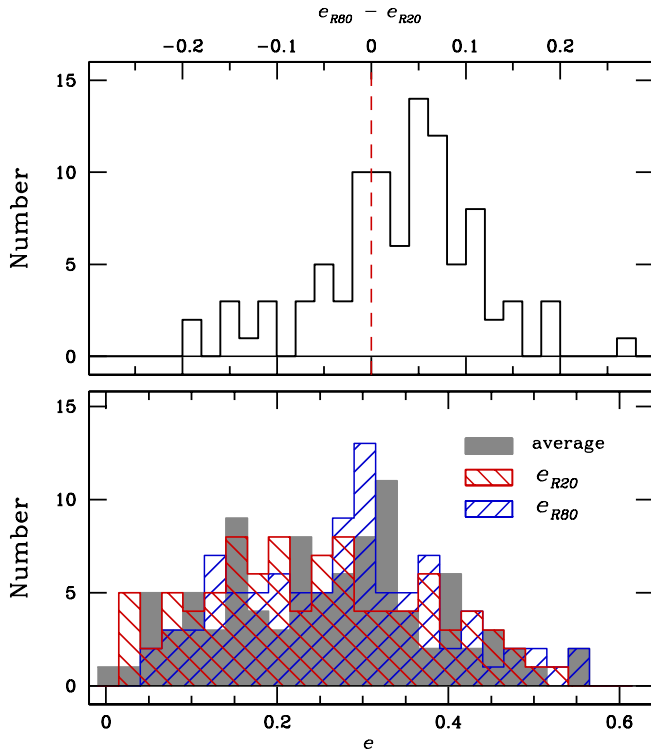


**Figure 20.** Bottom: distribution of the ellipticity averaged over the whole galaxy and as measured at two radii,  $R_{20}$  and  $R_{80}$ . Top: distribution of the ellipticity difference between  $R_{80}$  and  $R_{20}$ . The red dashed line marks zero. The outer regions are generally more flattened than the inner regions.

(A color version of this figure is available in the online journal.)

more reliable, and its interpretation (global lopsidedness) is the least ambiguous. Given the overall symmetry of our elliptical galaxies, we expect—and find—that the amplitude of the  $m = 1$  Fourier mode for each component to be very small. We also find

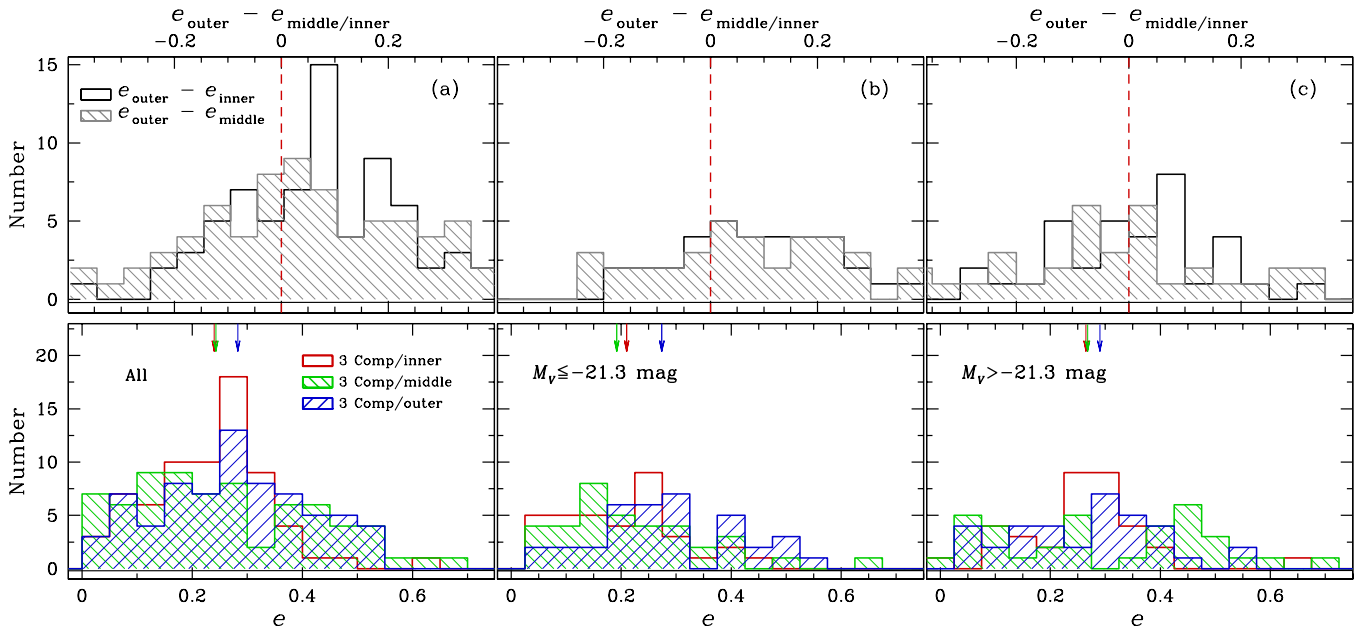
that the  $m = 1$  Fourier mode is actually not very sensitive to low-surface brightness features found in the outskirts of ellipticals. Faint tidal features contribute little to the global lopsidedness. Properly fitting these features would require higher-order modes or additional model components, which is beyond the scope of this work.

Figure 23 shows the distribution of the parameter  $A_L$ , defined as the absolute value of the amplitude of the  $m = 1$  Fourier mode (Equation (24) of Peng et al. 2010), calculated for both single- and multi-component models. Not surprisingly, the individual subcomponents attain systematically higher values of  $A_L$  than the global, single-component fit, because they are more sensitive to local perturbations. However, we find that not all high- $A_L$  components actually correspond to strong lopsidedness; instead, in some cases they seem to arise from different sources of contamination.

#### 4.2. Photometric Scaling Relations

Galaxies follow a number of scaling relations, whose slope and scatter provide insights to diagnose their formation and evolution. Among these relations, the ones that involve purely photometric parameters have been used most extensively as tools for understanding the structure of different types of galaxies. The mutual correlations among luminosity, effective radius ( $R_e$ ), and surface brightness at the effective radius ( $\mu_e$ ) have been most frequently used to reveal the physical connections within the family of hot stellar systems. K09 (and references therein) extensively apply this tool to understand the relationships between ellipticals, bulges, and spheroidals, and Kormendy & Bender (2012) extend this analysis to the subcomponents within S0 galaxies. In this section, we use these very same tools to explore the physical nature of the three subcomponents in ellipticals.

We begin by verifying that the CGS ellipticals comply with the global photometric scaling relations obeyed by other samples



**Figure 21.** Ellipticity of the galaxies fit with a three-component model, grouped into (a) the entire sample, (b) high-luminosity galaxies with  $M_V \leq -21.3$  mag, and (c) lower luminosity galaxies with  $M_V > -21.3$  mag. For each group, the bottom panel gives the  $e$  distribution of each of the subcomponents, with the respective median value indicated by arrows, and the top panel shows the difference between  $e$  for the outer and middle/inner components. Note that it is the high-luminosity objects that have a flattened outer component.

(A color version of this figure is available in the online journal.)

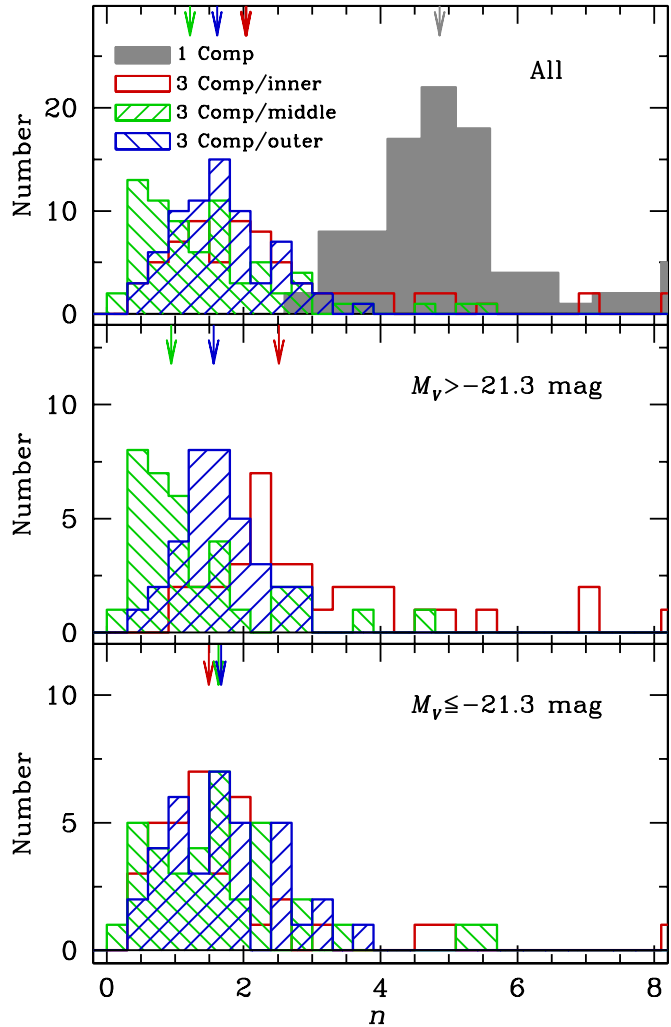


**Figure 22.** Distribution of Sérsic index  $n$  for the entire sample and then separately for the low-luminosity and high-luminosity groups. The top panel also includes the distribution of  $n$  for the single-component models.

(A color version of this figure is available in the online journal.)

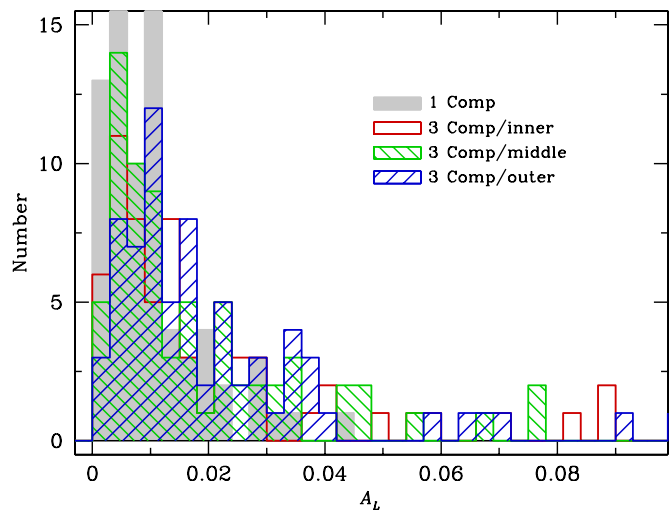


**Figure 23.** Distribution of the global asymmetry index,  $A_L$ , defined as the absolute value of the amplitude of the  $m = 1$  Fourier mode, shown separately for the subcomponents of the three-component fits and the single-component fits.

(A color version of this figure is available in the online journal.)

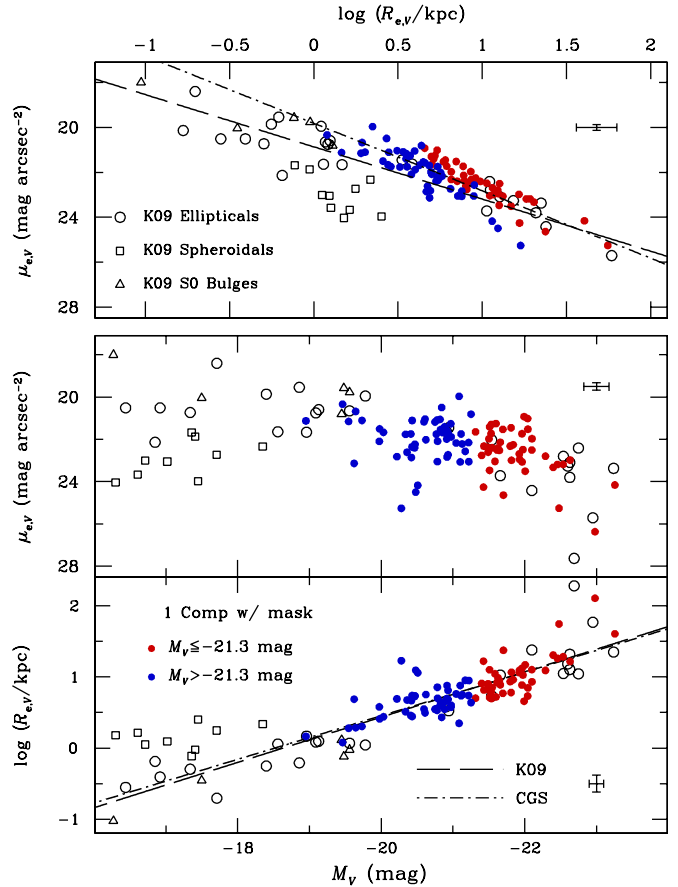


**Figure 24.** Correlations among luminosity, effective radius, and effective surface brightness for the 94 CGS ellipticals, compared to the sample of early-type (elliptical, spheroidal, and SO) galaxies from K09. For consistency with K09’s approach, we fit our galaxies using a single-component Sérsic model with a central mask applied. We divide our sample into high-luminosity ( $M_V \leq -21.3$  mag; red points) and low-luminosity ( $M_V > -21.3$  mag; blue points) groups. Representative uncertainties are given in the panels. The lines on the  $\mu_e$ – $R_e$  and  $M_V$ – $R_e$  plots are linear least-squares fits to the K09 and CGS samples.

(A color version of this figure is available in the online journal.)

of well-studied early-type galaxies. This comparison is made in Figure 24, where we use the sample of K09 as reference. For consistency with K09’s approach, we show single-component fits with a central mask, although the results without a central mask are very similar. Our objects do not extend to the lowest luminosities covered by K09’s sample, but over most of the luminosity range in which they do overlap the two samples follow very similar, tight correlations in the  $M_V$ – $R_e$  and  $R_e$ – $\mu_e$  plots; their formal linear least-squares fits (dashed and dot-dashed lines) are consistent. The distributions of the two samples also show good agreement in the  $M_V$ – $\mu_e$  plane. It is worth noting that in these plots the high- and low-luminosity subsamples merge seamlessly without any systematic differences in slope or scatter.

Figure 25 repeats this sequence of plots, but now showing each of the three subcomponents separately. The linear least-squares fits for the K09 sample are shown for reference in the  $M_V$ – $R_e$  and  $R_e$ – $\mu_e$  plots. Unlike K09, we do not circularize the  $R_e$  values, but this difference is only significant for components with high ellipticity; we highlight the points with  $e > 0.6$ , as well as those with relative uncertainties larger than 30%. The purpose of this exercise is twofold. First, we wish to establish whether the individual subcomponents identified in our fits

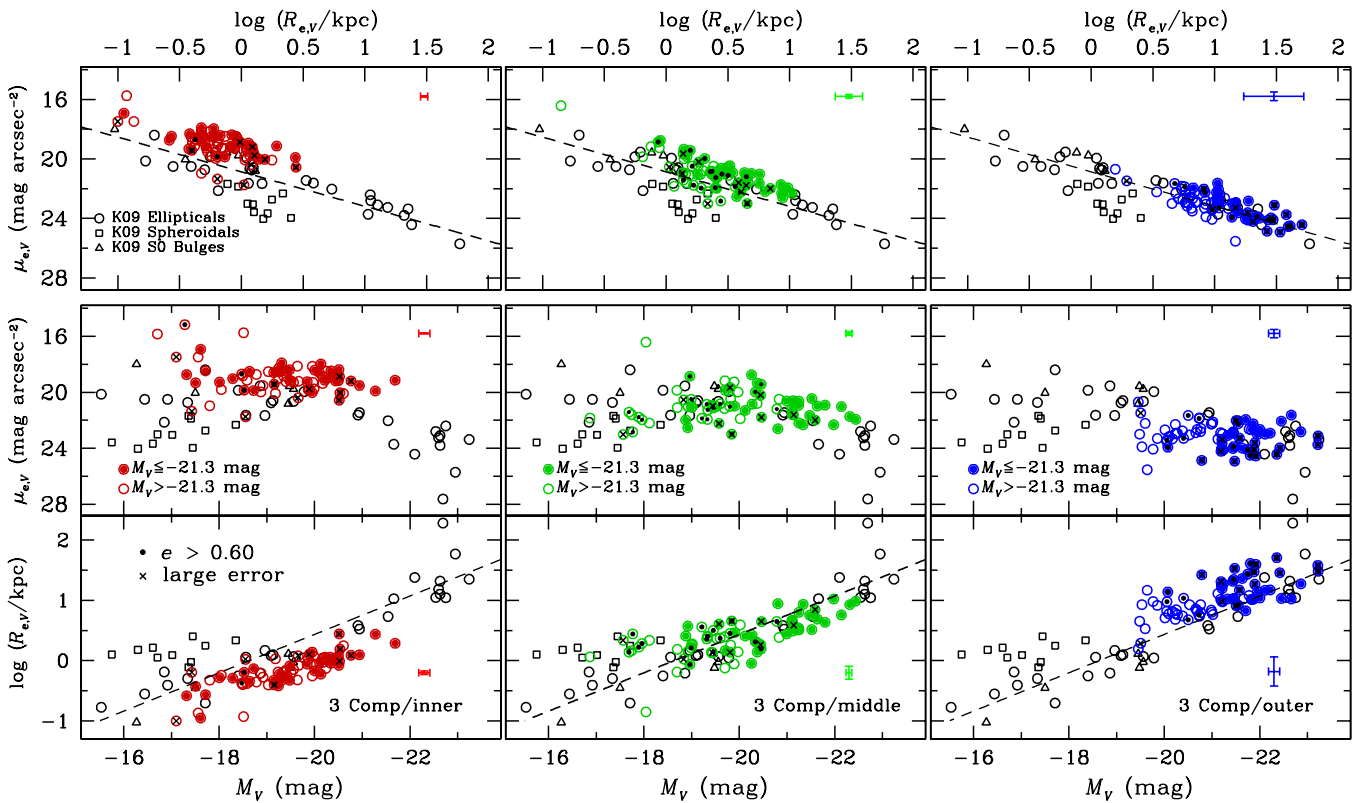


**Figure 25.** Correlations among luminosity, effective radius, and effective surface brightness for each of the subcomponent in the three-component models (left: inner; center: middle; right: outer). The typical uncertainties for these properties are illustrated using the error bar on the right side of each plot; points with the largest uncertainties are marked with a black cross. Components with  $e > 0.6$  are further highlighted with a small black dot. The CGS sample is divided into two luminosity groups, denoted by the solid ( $M_V \leq -21.3$  mag) and open ( $M_V > -21.3$  mag) colored points. As in Figure 24, data from K09 are overplot for reference; the dashed lines are linear least-squares fits to the K09 ellipticals.

(A color version of this figure is available in the online journal.)

follow any trends in these photometric scaling relations. If, for example, the subcomponents have no physical significance but are merely artifacts of decomposition, we would not expect them to display any coherent, let alone tight, relations. Second, if well-behaved patterns do indeed emerge, we hope to use them to gain insights into the physical nature of the subcomponents, in much the same way as these relations have helped to guide our understanding of the physical processes governing various types of galaxies (Kormendy 1985; Bender et al. 1992; Burstein et al. 1997; K09) and major substructures within them (e.g., Kormendy & Bender 2012). We summarize the key points to note the following.

1. The three major subcomponents *do* follow well-defined loci in the  $M_V - R_e$ ,  $R_e - \mu_e$ , and  $M_V - \mu_e$  planes.
2. The inner component occupies a region of parameter space similar to that populated by the lowest luminosity ellipticals and the classical bulges of S0 galaxies. The correlations for the high- and low-luminosity subsamples are equally tight. It is especially tight for the luminosity–size relation, where the slope seems to be flatter than that of the global relation.
3. The middle components of the high-luminosity sources define tight relations in the  $M_V - R_e$  and  $M_V - \mu_e$  planes that closely track the global ones. By contrast, low-luminosity sources contain middle components that overlap surprisingly closely with the locus of spheroidal galaxies. The same trend is present, albeit more subtly, in the  $R_e - \mu_e$  plot; at a fixed  $R_e$ , the low-luminosity group is displaced toward lower surface brightnesses, in the general direction

of spheroidals. Recall that the middle component of low-luminosity ellipticals exhibits attributes (low Sérsic indices, high ellipticity, occasionally dust features) reminiscent of disks (Section 4.1).

4. The outer component behaves very similarly for both luminosity groups. The most noticeable (but predictable) feature is their offset relative to the global luminosity–size relation: At fixed  $V$ -band luminosity, the outer components have larger  $R_e$  than predicted from the correlation based on global properties. The scatter is also larger, and the slope is marginally flatter. A formal linear least-squares fit for the entire sample results in  $M_V(\text{mag}) = (-3.76 \pm 0.65) \log R_e(\text{kpc}) - (0.23 \pm 0.03)$ , to be compared with  $M_V(\text{mag}) = (-6.14 \pm 0.48) \log R_e(\text{kpc}) - (0.33 \pm 0.03)$  for the combined collection of ellipticals and S0 bulges from K09. As for the  $R_e - \mu_e$  relation, the outer components are found to follow a very similar relation with the one defined by the global properties of elliptical galaxies. Although the scientific background is different, it is worth mentioning here that in Zaritsky et al. (2006), the even more extended intra-cluster light components of nearby galaxy clusters were found to exhibit a tight correlation between the effective radius and the mean surface brightness within that radius. The slope of such relation is also very similar to the one defined by the brightest cluster members. Although the outer components in this work are in general different from the intra-cluster stellar component, it is tempting to see that their properties are both closely tied to the global ones, which might indicate something in common regarding their

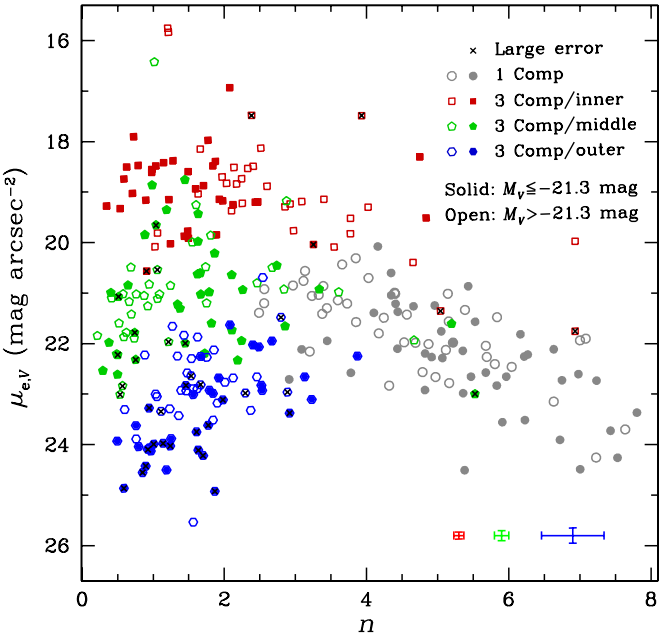


**Figure 26.** Correlation between Sérsic index and the surface brightness at the effective radius. We show the results for single-component fits and each of the subcomponents of the three-component models. Points with large uncertainties are marked with a black cross, and the two luminosity groups are denoted by the solid ( $M_V \leq -21.3$  mag) and open ( $M_V > -21.3$  mag) symbols. Typical error bars are given on the bottom-right corner of the plot.

(A color version of this figure is available in the online journal.)

origin. It is also interesting to note that the distribution of the outer component in the three planes shares some similarities with the trends for the *disks* of S0 galaxies, as presented by Kormendy & Bender (2012; see their Figure 17). While we do not suggest that the outer component of ellipticals are strictly analogous to S0 disks, it is intriguing that their isophotes do tend to be somewhat flattened (Section 4.1).

Apart from the primary mutual relations involving luminosity, size, and surface brightness, some studies have explored additional correlations involving the Sérsic index. Caon et al. (1993) and Trujillo et al. (2001), for example, discuss the general tendency for the Sérsic index to rise with increasing effective radius and decreasing effective surface brightness. As previous investigations were based on global Sérsic indices measured from single-component fits, it is worth revisiting this issue using the newly derived indices based on our subcomponent decomposition, which we have shown to be significantly different from those obtained from traditional fits. While our single-component fits do indeed recover the inverse correlation between Sérsic  $n$  and  $\mu_e$  (Figure 26, gray points), it is clear that, with the possible exception of the inner component of the low-luminosity subsample, the correlation completely disappears for the separate subcomponents. The uncertainties of the individual Sérsic indices are considerable (typical error bars shown on the lower-right corner of plot), especially for the outer component, but they cannot account for the huge observed scatter.

The redistribution of the Sérsic indices from large (e.g.,  $n \gtrsim 4$ ) to small values can be understood as a simple consequence of the behavior of the Sérsic function. A Sérsic profile with a high  $n$  has both a centrally concentrated core *and* an extended envelope. In this study, we promote the notion that the light distribution of ellipticals, particular the most luminous ones, separates into three portions that occupy small, intermediate, and extended

scales. Whereas the global profiles of these systems were once characterized by a single Sérsic function with large  $n$ , in our new description the compact and extended subcomponents each naturally accommodate a lower value of  $n$ . Galaxies with the highest luminosity and mass (and, via the above-described scaling relations, the largest  $R_e$  and lowest  $\mu_e$ ) traditionally have had the largest values of Sérsic  $n$  because they are the systems that have managed to build up an extended envelope. In the next paper of this series, this viewpoint will be explored in the context of the many recent efforts to quantify the evolution of the size and global Sérsic index of massive early-type galaxies.

#### 4.3. The Stellar Mass–Size Relation

The stellar mass–size relation offers another important diagnostic tool to investigate the formation and assembly of galaxies, both at low and high redshifts. In the local universe, it is well known that early-type galaxies follow a steeper stellar mass–size relation than late-type galaxies (Shen et al. 2003; Guo et al. 2009). This difference points to potentially different formation physics and evolutionary pathways. We wish to examine the stellar mass–size relation in light of our three-component decomposition of ellipticals.

For this analysis we need stellar masses. While accurate stellar masses are difficult to estimate for galaxies, the relatively massive, local elliptical galaxies in the luminosity range of our sample have roughly uniformly old stellar population (e.g., Kuntschner 2000), which, to a first approximation, can be assumed to have a single stellar mass-to-light ratio ( $M/L$ ). This assumption enables us to estimate reasonable stellar masses using empirical relations between broad-band optical colors and stellar  $M/L$ . Different colors and choice of models, which depend on the stellar population library, initial mass function, and star formation history, can lead to systematically different masses. As there is no clear evidence as to which combination is superior, we take the median of six mass estimations using the  $B-V$  and  $B-R$  relations from Bell & de Jong (2001), Bell et al. (2003), and Zibetti et al. (2009). The standard deviation of these six estimates is taken to be the uncertainty, which on average is 0.11 dex for  $\log M_*$ . To estimate stellar masses for the subcomponents, whose colors are not yet robustly known, we need to make an additional assumption that they have the same  $M/L$  as the global value. Considering that the observed optical color gradients of the ellipticals are quite weak (Papers I and II), this is probably not an unreasonable assumption. In any case, the errors incurred from assuming a constant  $M/L$  most likely do not exceed those associated with the image decomposition.

Figure 27 plots the final stellar masses versus  $V$ -band total absolute magnitude. The high- and low-luminosity subsamples are well separated in stellar mass. The median  $V$ -band luminosity ( $M_V = -21.3$  mag) used to separate the two luminosity subsamples translates to  $M_* = 1.3 \times 10^{11} M_\odot$ . In Figures 28 and 29, the stellar mass–size and stellar mass–luminosity fraction relations are shown. Our single-component fits recover a stellar mass–size relation that agrees with the relation defined by early-type galaxies in Guo et al. (2009). For this comparison, we use the fits without a central mask; the fits that include a central mask yield a relation with somewhat smaller scatter but that still agrees well with that of Guo et al. (2009).

The following trends emerge for the individual subcomponents.

1. The inner components of the high-luminosity ellipticals delineate a surprisingly tight sequence in the  $M_*$ – $R_e$  plane.

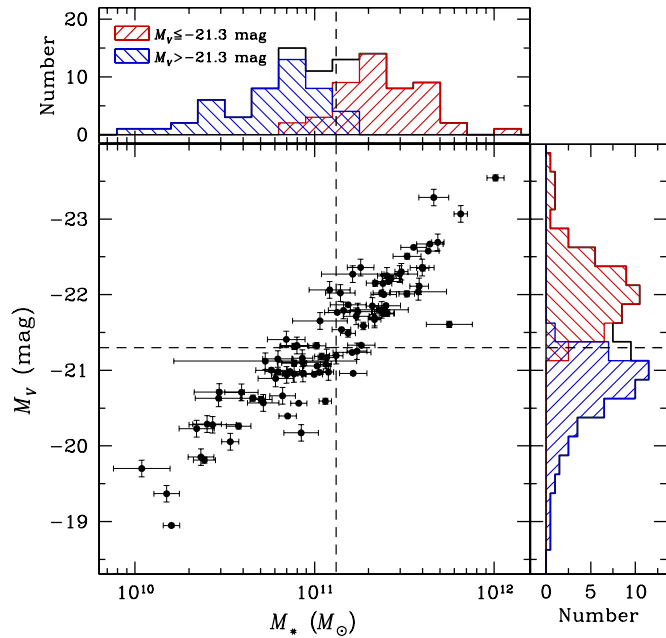


**Figure 27.** Distribution total  $V$ -band absolute magnitude vs. stellar mass, estimated from the optical colors as described in Section 4.3. The final adopted mass for each galaxy is the median of the estimates based on different colors and mass-to-light ratio relations, and the uncertainty is taken to be the scatter among these different estimates. The median value of  $M_V = -21.3$  mag corresponds to a median mass of  $M_* = 1.3 \times 10^{11} M_\odot$ . Throughout the paper, we define the high-luminosity and low-luminosity groups according to the median luminosity of the sample.

(A color version of this figure is available in the online journal.)

It runs approximately parallel to, but is significantly offset below, that of the global relation for early-type galaxies. Aside from the somewhat larger scatter, the same pattern can be seen for the lower-luminosity systems. At a fixed stellar mass, the inner component achieves much higher densities than the global average.

2. The behavior of the middle component is significantly different for the two luminosity groups. For the high-luminosity subsample, the middle component, with the exception of a few low-mass outliers, defines a tight  $M_* - R_e$  correlation that lies essentially on top of the best-fit relation for early-type galaxies from Guo et al. (2009). By contrast, the points for the low-luminosity subsample show not only much more scatter but also a shallower slope, one that roughly resembles that delineated by the late-type SDSS galaxies (Guo et al. 2009). In view of the disky nature of the middle component in low-luminosity ellipticals (Section 4.1), perhaps this similarity is to be expected.
3. The outer component in both luminosity groups occupies a distinct sequence offset above the global relation: At fixed mass, the most extended envelope is significantly more diffuse than the global average. The scatter is also notably larger, perhaps reflecting the stochastic nature in which this component was assembled or a more protracted history of formation.

## 5. THE PHYSICAL NATURE OF THE SUBCOMPONENTS

A large body of the current literature on elliptical galaxies is built on the notion that they have a highly concentrated global structure that can be well described by a Sérsic profile with a high index. Historically, this impression arose from the

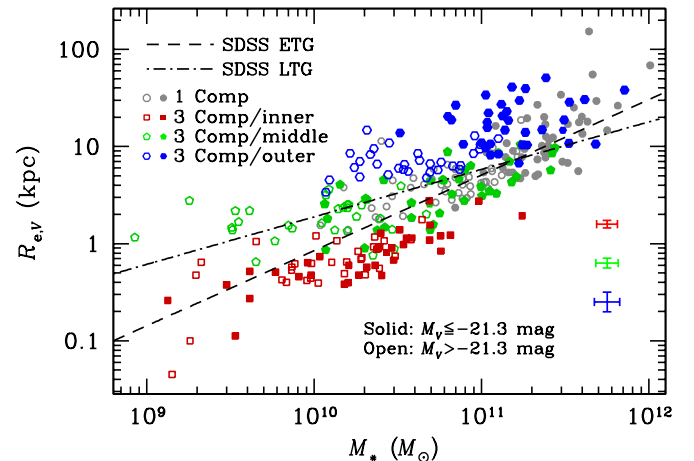


**Figure 28.** Dependence of the size of the different subcomponents on the total stellar mass of the galaxy. For reference, we also show the single-component models. The two luminosity groups are denoted by the solid ( $M_V \leq -21.3$  mag) and open ( $M_V > -21.3$  mag) symbols. The lines show the stellar mass-size relation for early-type galaxies (ETG) and late-type galaxies (LTG) derived from the SDSS analysis of Guo et al. (2009). Typical error bars are given on the bottom-right corner of the plot.

(A color version of this figure is available in the online journal.)

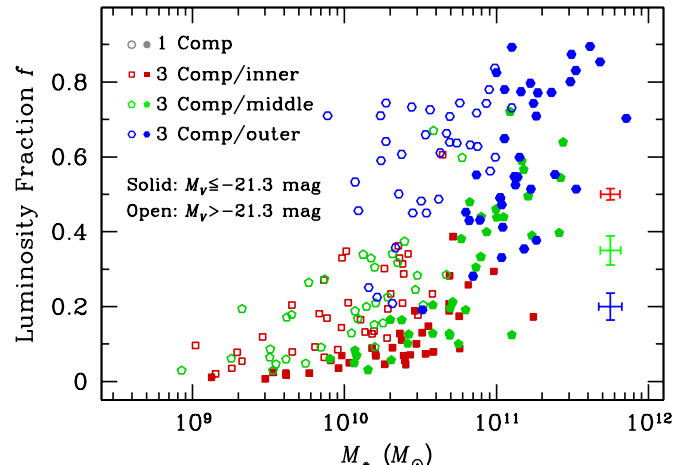


**Figure 29.** Dependence of the luminosity fraction of the different subcomponents on the total stellar mass of the galaxy. Typical error bars are given on the bottom-right corner of the plot.

(A color version of this figure is available in the online journal.)

common practice of fitting the surface brightness distribution using a single component, almost always using azimuthally averaged 1D light profiles. Abandoning the traditional 1D fits in favor of the more powerful 2D approach and taking advantage of the improved capabilities afforded by the latest version of GALFIT, we demonstrate in this work that nearby ellipticals, on scales of a few hundred pc to tens of kpc, can be decomposed into three distinct components on small ( $\lesssim 1$  kpc), intermediate ( $\sim 3$  kpc), and large ( $\sim 10$  kpc) scales. We show that these subcomponents obey well-defined scaling relations on the photometric fundamental plane and in the stellar mass-size relation. Below we argue that they provide “fossil records” that help decode the formation and evolutionary history of massive galaxies.

We are by no means the first to recognize that elliptical galaxies contain internal complexity or that their global profile cannot be modeled entirely using a single analytic function. The inner regions of ellipticals have long been known to depart from

the inward extrapolation of the outer global profile (Kormendy 1985; Lauer 1985). Ever since the advent of high-resolution observations from the *HST*, these central “deviations” have been commonly characterized using either a double power-law function (Ferrarese et al. 1994) or a “Nuker” law (Lauer et al. 1995). Low-luminosity ellipticals typically have steeper central power-law cusps<sup>13</sup> than the shallower cores found in high-luminosity systems (Faber et al. 1997; Ravindranath et al. 2001; Lauer et al. 2007). Regardless of the exact details, the canonical paradigm depicts ellipticals largely as a single-component system, most frequently described by a Sérsic function over most of its radial extent. Departures from this basic form, if they exist (Graham et al. 2003), only enter as perturbations near the center (Trujillo et al. 2004; Ferrarese et al. 2006; K09). At the other extreme in scale, studies of brightest cluster galaxies have shown that their outer regions often possess extended emission in excess of the outward extrapolation of an  $r^{1/4}$  law (Schombert 1986) or a Sérsic function (Graham et al. 1996; González et al. 2005; Donzelli et al. 2011). However, the prevailing perception has been that these extended envelopes are confined to the rarest, most massive ellipticals in clusters.

Here we propose that *most*, perhaps all, massive ellipticals possess three principal subcomponents that are physically distinctive. Ordinary, run-of-the-mill ellipticals generically contain a compact core, an intermediate-scale main body, and an extended outer envelope. The challenge now is to see whether a natural theoretical framework can be found to explain this substructure.

### 5.1. Inner Component: Evidence of Dissipation

The innermost compact component identified in our decomposition is directly analogous to the central structure revealed in *HST* images. Despite the inferior PSF of our ground-based images, the resolution of the CGS data suffices to isolate the central component as a photometrically distinct entity, even if its detailed shape may be poorly determined. At *HST* resolution the slopes of the central profile correlate with galaxy luminosity. Lower luminosity galaxies possess steep “extra-light” or “power-law” cusps, more luminous systems have flatter “cores,” and relatively few cases fall in between (Gebhardt et al. 1996; Faber et al. 1997; Ravindranath et al. 2001; Lauer et al. 2007; K09).<sup>14</sup> Our decomposition, interestingly, recovers a qualitatively similar trend. From Table 2, we find that low-luminosity subsample has a median Sérsic index of 2.6, which corresponds to a steeper inner profile than  $n = 1.5$ , the median Sérsic index for the high-luminosity members. The surface brightness distribution of ellipticals at *HST* resolution is usually parameterized in terms of a power-law slope. To compare our results with those from previous *HST*-based studies, we generated Sérsic profiles with the above median indices and, following Lauer et al. (2007), measured the central logarithmic slopes  $\gamma'$  within the inner 3''. For the high-luminosity subsample, the median (mean)  $\gamma' = 0.16$  (0.24), whereas the corresponding value for the low-luminosity sources is  $\gamma' = 0.42$  (0.58). While the exact value of  $\gamma'$  depends weakly on the chosen fitting region, the conclusion that more luminous ellipticals have flatter, less cuspy inner profiles than lower luminosity ellipticals is robust. Indeed, our CGS-derived measurements of  $\gamma'$  are surprisingly close to the typical values for the “core” and “cusp” subsamples from

<sup>13</sup> K09 advocate changing the nomenclature from “power-law” to “extra-light.”

<sup>14</sup> This issue remains contentious (Ferrarese et al. 2006; Glass et al. 2011).

Lauer et al. (2007), although we are not confident enough in our ground-based measurements to judge whether the inner slopes are truly dichotomous with respect to the galaxy luminosity. It is noteworthy that the parameter correlations for the inner component on the photometric fundamental plane show very similar behavior (Figure 25) for the two luminosity subsamples. At the same time, the stellar mass–size relation of the inner component for lower luminosity ellipticals does exhibit slightly larger scatter at the low-mass end (Figure 28).

A crucial distinction between our results and those of previous studies is that we do not necessarily regard the central component as a continuous extension or modification of an exterior component. In our decomposition the central substructure is simply a separate component that naturally emerges from the fits.

In a series of works based on hydrodynamical simulations of gas-rich galaxy-galaxy mergers, Hopkins et al. (2009a, 2009b, 2009c) presented a two-component model to unify the global and central structure of elliptical galaxies. In their picture, the extra-light or power-law component is the relic of a dissipational starburst resulting from a gas-rich merger event. Subsequent mergers of these now gas-poor, extra-light ellipticals preserve this central dense, compact component, until the newly formed binary black hole scours the central density profile into an even flatter, lower density core. Hopkins et al. (2009a, 2009c) fit the 1D profiles of their simulated galaxies and the observational data of a sample of both “core” and “cusp” elliptical galaxies using an inner exponential plus a single, outer Sérsic component. Their choice to use an exponential profile for the central component is partly due to the limited resolution of their simulations and partly motivated by the starburst nature of their model. The results of our study show that this assumption is too restrictive and unnecessary. Within our low-luminosity subsample, the best-fitting Sérsic indices have an average value of  $n = 3.2$ , a standard deviation of 2.1, and a median value of 2.6. Forcing the central component to a Sérsic index that is lower than it actually should be will bias the outer Sérsic component to a higher index. This contributes, in part, to the systematically higher Sérsic indices, compared with our values, that Hopkins et al. (2009a) obtained for the main body of the galaxy. The second, more dominant reason why our Sérsic indices are much lower is that we have split the main body of the galaxy into two pieces, in our nomenclature dubbed the middle and outer components, which individually have lower Sérsic indices (median  $n = 0.9$ –1.6) than when summed into a single entity. Apart from this difference, our inner component strongly resembles the extra-light component in the Hopkins et al. (2009a) models. In both cases, for instance, the size scale is  $\lesssim 1$  kpc, and the luminosity (mass) fraction is  $\sim 10\%$ . The inner component of the high-luminosity subsample in our study has about a factor of 2 lower luminosity fraction (median  $f = 0.08$ ) than in the low-luminosity subsample (median  $f = 0.19$ ), qualitatively consistent with the expectation from Hopkins et al. (2009c, their Figure 21), but in neither group does the luminosity fraction drop with increasing galaxy mass (see Figure 29).

### 5.2. Middle Component: Embedded Disks and Compact Nuggets

The physical nature of the middle component depends on the galaxy luminosity. Although some overlap inevitably arises from our semi-arbitrary division of the sample into two luminosity groups, the middle component in low-luminosity sources is more heterogeneous and qualitatively different from that in the

high-luminosity subsample. Its distribution within the photometric scaling relations (Figure 25) shares qualitative and quantitative similarities with the loci populated by spheroidals (K09, their Figure 37) and the disks of late-type spirals (Kormendy & Bender 2012, their Figure 20), and its stellar mass–size relation (Figure 28) broadly resembles that of late-type (i.e., disk-dominated) galaxies. Additional evidence for the disk-like nature of the middle component in low-luminosity sources comes from their near-exponential profile (median  $n = 0.92$ ; Table 2), their relatively high ellipticity (median  $e = 0.27$ ), and the frequent detection of dust-like small-scale features in their residual images. It is important to recognize that this embedded disky component is not a minor perturbation to the overall structure of low-luminosity ellipticals. On average it accounts for  $\sim 20\%$  of the  $V$ -band luminosity. With a typical effective radius of  $R_e \approx 2.5$  kpc, which for an  $n = 1$  Sérsic function translates to a scale length of  $h = R_e/1.678 = 1.5$  kpc, these disky structures should not be confused with nuclear or circum-nuclear disks identified through dust absorption or line emission in *HST* images (e.g., Harms et al. 1994; Tomita et al. 2000; Tran et al. 2001), which are much more compact. Nor are they equivalent to the extended disks familiar in S0 galaxies, which have  $h \approx 1\text{--}10$  kpc (Laurikainen et al. 2010), with a median value of 3.2 kpc. Instead, the disk-like component isolated in our study is none other than that responsible for producing the disky isophotes that have long been known to be common in ellipticals of lower luminosity (e.g., Carter 1978; Lauer 1985; Bender & Möllenhoff 1987; Bender 1988; Franx et al. 1989; Peletier et al. 1990). Our decomposition enables this component to be extracted and studied quantitatively. The most straightforward interpretation for these structures is that they are remnants of dissipative mergers, along the lines discussed by Hopkins et al. (2009a, 2009b, 2009c).

We believe that the middle component in high-luminosity galaxies has a very different physical origin. In terms of gross properties, it is physically larger (median  $R_e = 3.5$  kpc), rounder ( $e = 0.20$ ), more centrally concentrated ( $n \approx 1.6$ ), and occupies  $\sim 20\%$  of total luminosity. It delineates a tight sequence in the photometric scaling relations and in the stellar mass–size plane. As discussed in S. Huang et al. (2013, in preparation), in many ways the combination of the inner and middle components for high-luminosity ellipticals resembles the compact, massive galaxies dubbed “red nuggets” at high redshifts (e.g., Damjanov et al. 2009).

### 5.3. Outer Component: Extended Envelope

As mentioned earlier, in its most extreme form extended envelopes have long been known to exist in brightest cluster galaxies. The CGS sample, however, has but two brightest cluster galaxies—NGC 1399 in Fornax and NGC 4696 in the Centaurus Cluster. Most of our ellipticals are indeed relatively luminous, but they are representative of the overall local elliptical galaxy population and are in no way biased by extreme objects. Yet, we find that present-day ellipticals almost always contain a large-scale, “puffed up” outer component. We detect this component in at least 75% of our sample, essentially independent of luminosity. The average properties of the extended emission in the two luminosity groups are qualitatively similar, but differ in detail. Although the two subsamples exhibit very comparable luminosity fractions ( $f \approx 0.6$ ), the high-luminosity objects have median  $R_e = 17.8$  and  $n = 1.6$ , to be compared with  $R_e = 6.6$  and  $n = 0.7$  for the low-luminosity sources. The envelopes of the more luminous

objects are also systematically more flattened, as discussed in Section 3.5 and illustrated in Figure 21. However, both subsamples form a more-or-less continuous sequence that sits distinctly offset from the global relations, from the sequences defined by the other two subcomponents in the photometric scaling relations (Figure 25), and in the stellar mass–size relation (Figure 28). Now, the scatter for the outer component in these diagrams is notably larger. Part of this surely can be blamed on the extra uncertainty associated with these difficult measurements (representative error bars are given in all the plots), but most of the observed increased scatter is probably intrinsic.

Inspection of Figure 18 from Kormendy & Bender (2012) reveals something intriguing: The distribution of points for the disks of S0 galaxies bears an uncanny resemblance to those for the outer component of our ellipticals. Is this apparent similarity just a coincidence or is it telling us something fundamental about common formation physics?

Much recent research draws attention to the dramatic size evolution experienced by elliptical galaxies. Observations (Bezanson et al. 2009; van Dokkum et al. 2010) show that massive early-type galaxies typically double in mass and triple in size from  $z \approx 1$  to  $z = 0$ . Most of the size growth takes place in the outskirts, through a series of minor, dissipationless mergers and hot-phase accretion (Naab et al. 2007, 2009; Oser et al. 2010, 2012). In the next paper of this series, we critically examine this model in light of our observations.

## 6. FUTURE DIRECTIONS

The perspective afforded by the multi-component nature of elliptical galaxies gives us a new window to investigate several other issues related to massive galaxies.

1. Many recent studies suggest that the massive galaxy population has undergone strong size evolution since its formation epoch. The most massive galaxies at  $z \approx 2.5$  appear old, dead, and much more compact than present-day galaxies of similar mass (e.g., Cimatti et al. 2004; McCarthy et al. 2004; Bezanson et al. 2009; van Dokkum et al. 2010). Minor, dissipationless mergers may govern how these “red nuggets” accumulate outer stellar envelopes so that their density profiles match those of local giant ellipticals (Naab et al. 2009; Oser et al. 2010). We explore this issue in a companion paper (S. Huang et al. 2013, in preparation).
2. The mass of supermassive black holes scales tightly with the properties of the spheroidal (bulge) component of the host galaxy, especially its stellar velocity dispersion (Gebhardt et al. 2000; Ferrarese & Merritt 2000), luminosity (Kormendy & Richstone 1995), and mass (Magorrian et al. 1998; Häring & Rix 2004). The observations of McConnell et al. (2011, 2012) suggest that the largest black holes in the most massive local ellipticals may deviate systematically from lower mass objects in their black hole mass–host relations. In light of the substructure identified in this study, it is interesting to ask whether any of the subcomponents in giant ellipticals actually correlate better with the black hole mass than the entire galaxy as a whole. To address this issue, we are in the process of applying our 2D decomposition technique to deep images of all ellipticals with dynamical detections of black holes.
3. Integral-field spectroscopy has revealed the great diversity of the kinematic properties of the central regions of early-type galaxies, which can be broadly classified as fast or slow

- rotators (Emsellem et al. 2007; Cappellari et al. 2011a). At the same time, the velocity structure in the far outer regions of ellipticals is also beginning to be explored with a variety of kinematic tracers (e.g., Coccato et al. 2009; Murphy et al. 2011; Pota et al. 2013; Romanowsky et al. 2012). What is the connection between the kinematic and photometric substructure?
4. Local elliptical galaxies are generally red and have gentle color gradients (e.g., La Barbera et al. 2010). If the subcomponents trace distinct episodes or modes of star formation or assembly, they may imprint measurable features in the global color distribution. An upcoming work will examine this problem using the rest of the CGS multi-band data.
  5. Globular cluster systems also carry important clues about the formation and evolutionary processes of their host galaxies. Bimodal or multi-modal color distributions are frequently observed, as are radial variations in their relative number density (Brodie & Strader 2006, and references therein). It would be fruitful to investigate the detailed 2D spatial distribution of globular clusters to ascertain whether there is any connection between different cluster populations and the structural components identified in this work.
  6. Our 2D decomposition has identified several possible misclassified S0 galaxies. It is interesting to note that a four-component model always provides a reasonably good description of their structure. We do not discuss the physical properties and nature of the subcomponents here, but we will return to this issue in a systematic analysis of all S0 galaxies in CGS.

## 7. SUMMARY

We present a comprehensive structural analysis of 94 representative, nearby elliptical galaxies spanning a range of environments and stellar masses ( $M_* \approx 10^{10.2} - 10^{12.4} M_\odot$ ). We use GALFIT 3.0 to perform 2D multi-component decomposition of relatively deep, moderately high-resolution  $V$ -band images acquired as part of the CGS. Extensive experiments were performed to devise an optimal strategy for determining the sky level and its uncertainty, which is one of the most important factors that influences the decomposition, to explore the consequences of PSF blurring in the nuclear regions, and to verify the robustness of our fitting strategy. The final models describe as much of the visible structures as possible using the minimum number of components with reasonable Sérsic parameters, while simultaneously minimizing the residuals and accounting for all the geometric constraints.

Our analysis challenges the conventional notion that the main body of giant ellipticals follows a single structure described by a high Sérsic index (e.g.,  $n \gtrsim 3$ –4). We propose that the global light distribution of the majority ( $\gtrsim 75\%$ ) of ellipticals is best described by three Sérsic components: a compact, inner core with typical effective radius  $R_e \lesssim 1$  kpc and luminosity fraction  $f \approx 0.1$ –0.15; an intermediate-scale, middle component with  $R_e \approx 2.5$  kpc and  $f \approx 0.2$ –0.25; and an extended, outer envelope with  $R_e \approx 10$  kpc and  $f \approx 0.6$ . The subcomponents have relatively low Sérsic indices, in the range  $n \approx 1$ –2. The middle components of lower luminosity sources typically exhibit the lowest values of  $n$ , consistent with other evidence (e.g., high ellipticity, disk-like scaling relations, dust features) that these systems often contain embedded stellar disks. The outer envelopes of high-luminosity ( $M_V \leq -21.3$  mag), high-

mass ( $M_* \gtrsim 10^{11} M_\odot$ ) objects are notably more flattened than the inner portions of the galaxy.

The three principal subcomponents identified in our image decomposition are robust features in bright, local elliptical galaxies. Our belief in their physical reality is bolstered by the fact that the individual subcomponents share a set of common, relatively homogeneous observational characteristics, that their structural parameters obey well-defined (and in some cases rather tight) photometric scaling relations, and that they follow distinct tracks on the stellar mass–size relation. Future papers in this series will take advantage of the perspective gained from this work to further shed light on the formation and evolutionary pathway of massive galaxies.

We thank the anonymous referee for helpful comments that improved this paper. This work was supported by the Carnegie Institution for Science (L.C.H.), the UC Irvine School of Physical Sciences (A.J.B.), the China Scholarship Council (S.H., Z.-Y.L.), and under the National Natural Science Foundation of China under grant 11133001 and 11273015 (S.H.). S.H. thanks Professor Q.-S. Gu and the School of Space Science and Astronomy in Nanjing University for providing long-term support. Funding for the SDSS and SDSS-II has been provided by the Alfred P. Sloan Foundation, the Participating Institutions, the National Science Foundation, the U.S. Department of Energy, the National Aeronautics and Space Administration, the Japanese Monbukagakusho, the Max Planck Society, and the Higher Education Funding Council for England. The SDSS Web site is <http://www.sdss.org>.

## APPENDIX A THE PSF AND THE RED HALO EFFECT

Michard (2002) and Wu et al. (2005) discuss the so-called red halo effect for images obtained using thinned CCDs, such as that employed for CGS. This instrumental effect adds an extended, halo-like feature to the wings of the PSF. The amplitude of this feature varies significantly with wavelength and is particularly pronounced in redder bandpasses (e.g.,  $I$  band). The red halo effect imprints low-level structure on the scale of the extended PSF wings on any sufficiently peaked and strong source, including the bright cores of galaxies. Not taking this effect into account in the analysis can potentially imprint spurious features on the brightness profiles of galaxies, on angular scales corresponding to the size of the PSF halo. Although the effect is most noticeable in the color profile, in principle it can also have some low-level impact on the surface brightness distribution. While it is unlikely that this PSF effect can strongly influence our image decomposition analysis, it would be prudent, if possible, to avoid this problem altogether because our main scientific goal hinges on measuring subtle internal substructure in elliptical galaxies.

We study the red halo effect using a method similar to that of Michard (2002). To create a PSF with sufficiently high signal-to-noise ratio to reveal its faint, extended wings, it is necessary to create a composite PSF image by combining the unsaturated wings of a very bright star with the unsaturated core of a fainter star. We searched for appropriate candidates from the large collection of CGS images, selecting candidate stars from regions of the image sufficiently far from the main galaxy to be unaffected by it. Figure 30 shows composite PSFs that extend out to a radius of  $\sim 100''$ , selected from three observations obtained

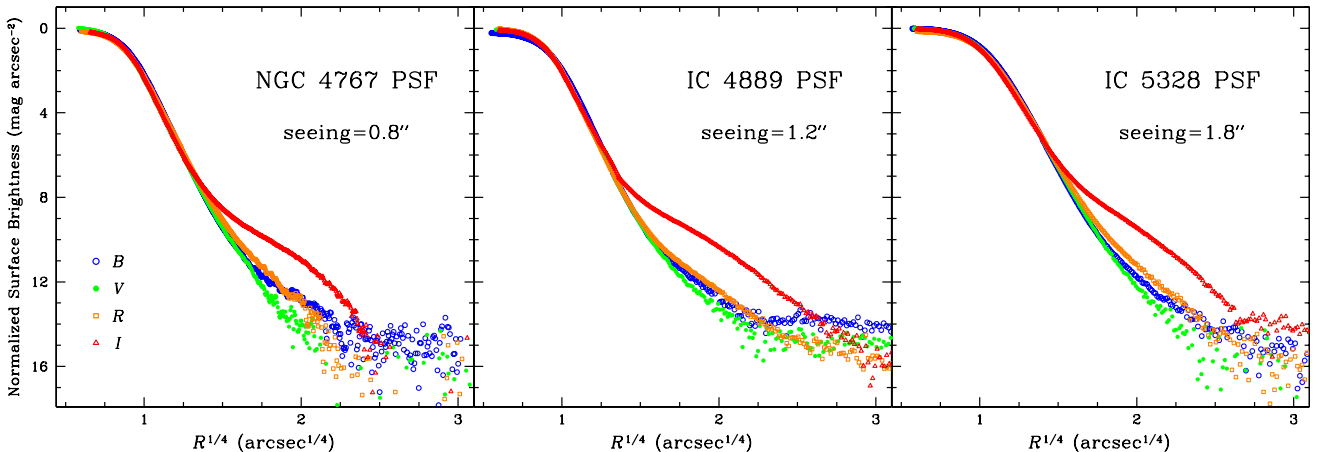


**Figure 30.** Radial profiles of the combined PSF for three stars (in different galaxies) that represent three different seeing conditions. The profiles from different bands are shown in different colors and symbols, after being normalized at  $2''$ . The red halo effect is clearly seen in the  $I$ -band PSF.  
(A color version of this figure is available in the online journal.)

under  $0''.8$ ,  $1''.2$ , and  $1''.8$  seeing. The PSFs for the four CGS bands have been normalized at a radius of  $2''$ .

The red halo effect is immediately obvious in the  $I$ -band PSF, which has a prominent, extended wing that extends from  $\sim 10''$ – $60''$ . To first order, both the amplitude and the shape of the red halo are independent of the seeing and, implicitly, of time because the three observations were taken over widely separated observing runs. However, due to the uncertainty of the sky background subtraction and the precision of PSF profile matching, it is not clear whether or not we can build a composite PSF model robust enough to be applicable to all the  $I$ -band observations. For this reason, we decided to omit the  $I$ -band images from the current analysis. No clear evidence of a similar halo effect is seen in the PSFs of the other three filters. Both the  $B$ -band and  $R$ -band PSFs show only a mildly extended wing, which seems altogether absent in the  $V$  band. We have thus chosen to focus only on the  $V$ -band images for the current analysis.

## APPENDIX B

### SKY BACKGROUND ESTIMATION

We estimate the level of the sky background by performing a multi-component 2D fit to the entire image. The galaxy is modeled with a series of Sérsic components (up to five), and the sky is included as a free parameter to be determined by the fit. After examining the suite of acceptable models, we choose as the final sky level the average of the sky values from all the acceptable fits.

An important factor that affects the accuracy with which the sky background can be estimated is the size of the image relative to the size of the galaxy. This is especially critical for elliptical galaxies whose outer light profile is usually very extended. When the galaxy extent occupies a significant fraction of the image, the sky determination will be strongly model-dependent. This problem has been tested by Yoon et al. (2011, see their Figure 23) using simulated galaxy images and single-component Sérsic models. These authors performed a comprehensive statistical analysis to quantify the dependence of the uncertainty of the sky background on the relative image size (in units of  $R_{50}$ ). The uncertainty increases with decreasing relative image size, especially when  $R_{\text{img}} \lesssim 5 R_{50}$ .

In contrast to Yoon et al. (2011), we propose that in real images the level of the sky uncertainty should be directly compared

to the intrinsic fluctuation of the background because the sky background is usually not flat, which translates into a measurement uncertainty. To measure the background fluctuation, we apply object masks and an aggressive mask for the main galaxy to the image and select a large number of small, unmasked, non-overlapping, box regions. As mentioned above, the sky is not flat and has fluctuations that cannot be masked out perfectly. In light of the non-flatness of the sky, each box serves as an independent measurement of the true sky. Under that assumption, the effective uncertainty of the sky background is the rms over all the measurements divided by the number of boxes:  $\sigma_{\text{sky,eff}} \approx \sigma_{\text{box}} / \sqrt{n_{\text{box}}}$ , where  $\sigma_{\text{box}}$  is the standard deviation of the mean pixel values from all the boxes and  $n_{\text{box}}$  is the number of useful boxes.

Factors such as the size of the boxes, the size of the mask for the central galaxy, and the number of boxes can affect these measurements. We test the impact of different choices. In the end, we choose to use  $1.8 R_{50}$  as the size for the galaxy mask, with an elliptical shape fixed to the axis ratio and PA given in Paper I. This value was selected based on a series of tests to ensure that the mask covers the most visible parts of the galaxy and leaves enough space for background estimation at the same time. We generate 120 random boxes for each image and then remove the ones that overlap; the final number of useful boxes is always around 100. When  $R_{\text{img}} \geq 6 R_{50}$ , we choose the box size to be  $30 \times 30$  pixels; for smaller relative image sizes we pick a box size of  $20 \times 20$  pixels to ensure a comparable number of boxes for both large and small images.

The sky estimates based on the technique proposed here should converge with the model-independent values in the limit when the image is large enough to permit the sky to be measured directly. We test this using a subsample of 30 ellipticals that satisfy  $R_{\text{img}} > 10 R_{50}$ , for which direct sky values are available from Paper I. We artificially reduce the relative image size by keeping the galaxy fixed at the center and progressively cropping the outer regions of the image to produce simulated images where  $R_{\text{img}} = 10, 8, 6, 5$ , and  $4 R_{50}$ . For each of these modified images, we fit models with 1 to 5 Sérsic components plus a sky background term. As our purpose here is to achieve the most realistic representation of the galaxy, the different Sérsic components are allowed to have different centers, and the  $m = 1$  Fourier mode is added to each of them.

It was immediately apparent from these tests that a single-component model is inadequate to recover a reliable sky

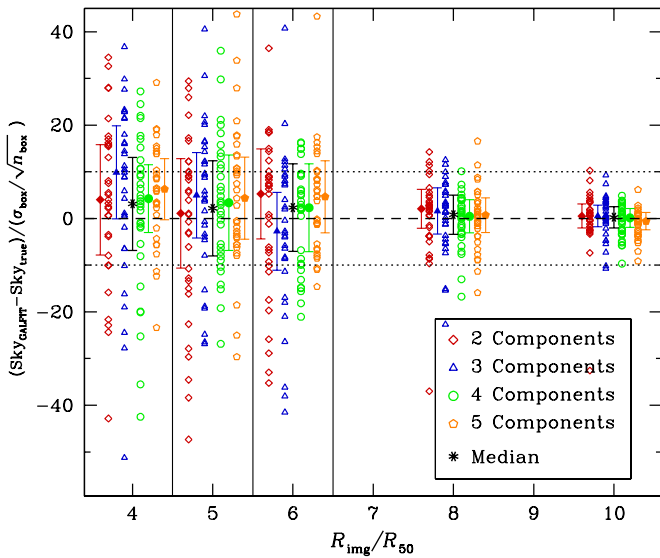


**Figure 31.** Dependence of the relative uncertainty of the sky value, expressed in units of the background fluctuation (denoted by  $\sigma_{\text{box}}/\sqrt{n_{\text{box}}}$ ; see Appendix A), on image size ( $R_{\text{img}}$ ), normalized to the half-light radius of the galaxy ( $R_{50}$ ). The uncertainty on the sky is empirically defined to be the difference between the model-dependent value obtained from our multi-component 2D fit (Sky<sub>GALFIT</sub>) and the model-independent, presumed true value (Sky<sub>true</sub>) directly measured from the outer regions of 30 angularly small galaxies. The open colored symbols denote models with different numbers of components (2–5); their median values and corresponding scatter are given by the solid symbols with error bars. For clarity, the different models are offset slightly along the  $X$ -axis. We analyze simulated images in five bins of relative image size:  $R_{\text{img}}/R_{50} = 4, 5, 6, 8$ , and  $10$ . The black asterisks (and corresponding error bars) represent the median value (and its scatter) of the four different models in each size bin. The black horizontal dashed line and the flanking dotted lines mark  $(\text{Sky}_{\text{GALFIT}} - \text{Sky}_{\text{true}})/(\sigma_{\text{box}}/\sqrt{n_{\text{box}}}) = 0.0 \pm 10$ .

(A color version of this figure is available in the online journal.)

background. The sky value from the single-component models deviates systematically from the true value, even when the image is very large. This just reflects the fact that a single Sérsic function gives a poor description of the light distribution of elliptical galaxies. For multi-component models, as shown in Figure 31, the scatter of the sky uncertainty strongly increases with decreasing relative image size ( $R_{\text{img}}/R_{50}$ ). However, for sufficiently large images, multi-component models can recover the intrinsic sky value with good accuracy. It is reassuring that there is little systematic offset even when the image is very small; the median uncertainties of the sky are all very close to zero for each image size bin and for models with different numbers of components. Careful examination reveals that the handful of extreme outliers in Figure 31 can be traced to models that are clearly incorrect. For example, when the effective radius or Sérsic index of one of the components is extremely large (e.g.,  $R_e > R_{\text{img}}$  or  $n > 10$ ), the sky value tends to be severely underestimated. This betrays an important disadvantage of our model-dependent method of sky estimation. Nevertheless, this weakness can be overcome by exploring a wide suite of models to seek out the subset that produces a consistent, stable solution for the sky background.

We apply this new procedure to the  $V$ -band images of the entire elliptical galaxy sample to obtain a uniform estimate of their sky background. Guided by the above tests, we no longer consider the single-component Sérsic models. The final sky value of each galaxy is taken to be the average of the best-fit sky values of all acceptable models, after excluding problematic cases, if any.

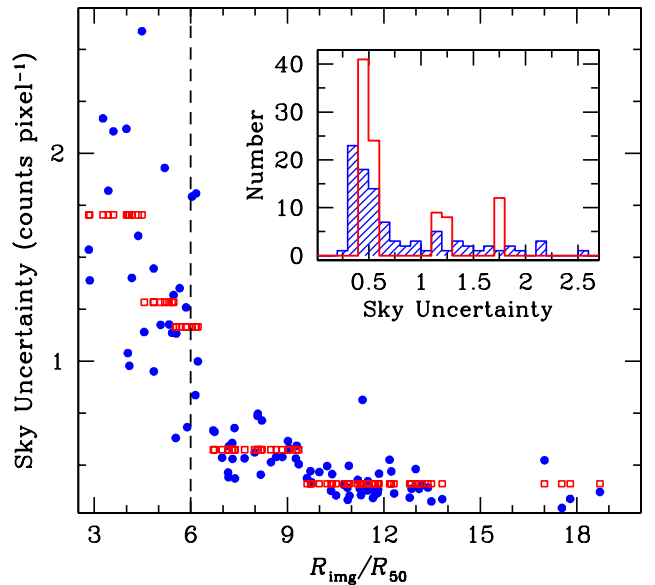


**Figure 32.** Relation between the new sky uncertainties and the relative image size. The sky uncertainties are calculated using the background fluctuation measured for each individual galaxy (blue dots) and the average background fluctuation in each image size bin (red squares). The distribution of the uncertainties is plotted in the inset figure; hatched blue histograms correspond to the individually measured background fluctuations, whereas the dashed red histograms denote the average values based on image size. The vertical dashed line marks  $R_{\text{img}}/R_{50} = 6$ , below which the sky uncertainties increase dramatically.

(A color version of this figure is available in the online journal.)

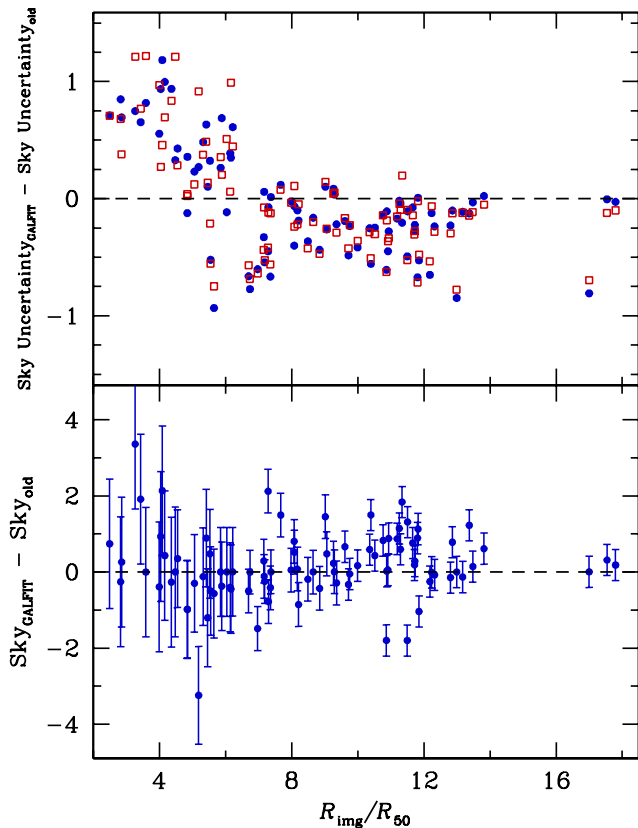
Since we express the average level of uncertainty of the sky in units of the background fluctuation (Figure 31), the corresponding uncertainty on the sky for each galaxy, in units of counts pixel<sup>-1</sup>, can be obtained by simply multiplying the measured background fluctuation in the image with the average sky calibration uncertainty for its image size bin. To obtain the sky uncertainty, we use both the background fluctuation measured for the individual galaxy and the average value for all ellipticals in the same image size bin. As shown in Figure 32, the resulting sky uncertainties agree well for both choices of background fluctuation values. The expected trend with relative image size is also very clear: The sky uncertainty increases dramatically with decreasing image size, especially when  $R_{\text{img}} \lesssim 6 R_{50}$ .

Figure 33 compares the new sky estimates and uncertainties with those originally calculated in Paper I. For the sky values, the difference between the new and old values shows no trends with the relative image size of the galaxy. However, the old values of the sky uncertainty for small galaxies ( $R_{\text{img}} \lesssim 6 R_{50}$ ) are on average systematically lower than the new values, by  $\sim 1.9$  counts pixel<sup>-1</sup>; for large galaxies, the trend is reversed, such that the original sky uncertainties are systematically overestimated (by approximately the same magnitude).

## APPENDIX C

### EXTERNAL CHECKS WITH SDSS

As in Paper II, we performed external checks of our 2D fits using images from the SDSS. The spatial resolution, seeing conditions, and photometric depth of the SDSS data are different from those of CGS. Six of the CGS ellipticals are in the SDSS DR8 catalog (Aihara et al. 2011). We retrieved their  $g$ -band images, the closest analogs to the CGS  $V$ -band data,



**Figure 33.** Comparison of the new, GALFIT-based sky values and uncertainties with the old values given in Paper I, plotted as a function of relative image size,  $R_{\text{img}}/R_{50}$ . The unit for both sky values and their uncertainties are counts. The top panel shows sky uncertainties calculated using the background fluctuation measured for each individual galaxy (blue dots) and the average background fluctuation in each image size bin (red squares). The error bars in the bottom panel reflect the typical sky uncertainty, calculated following our new method. (A color version of this figure is available in the online journal.)

from SDSS DR8 Data Access.<sup>15</sup> The SDSS images are already sky subtracted. We created objects masks and empirical PSF images using the same method for CGS. We fit the SDSS images with one- and two-component Sérsic models, starting

<sup>15</sup> [http://www.sdss3.org/dr8/data\\_access.php](http://www.sdss3.org/dr8/data_access.php)

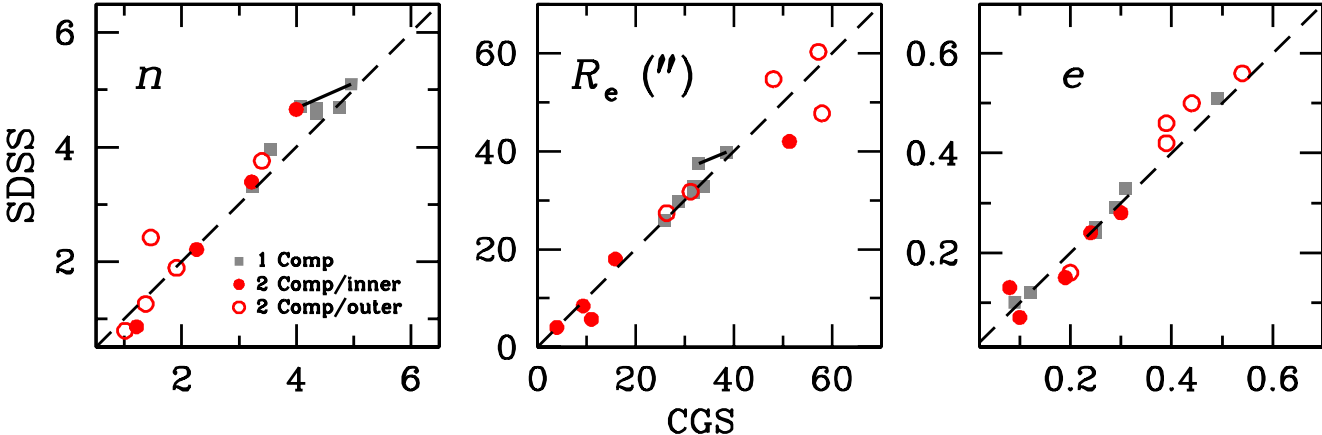


**Figure 34.** Comparison of one- and two-component models for six CGS galaxies that are in common with SDSS. The three panels show the fitted values of the Sérsic index, effective radius, and axis ratio; the dashed line indicates equality. Gray filled pentagons are from the one-component fits, and red filled circles and blue open circles represent the inner and outer components of the two-component fits, respectively. The two gray filled pentagons connected by a solid line are for NGC 1199; they represent fits with and without its central dust lane masked out.

(A color version of this figure is available in the online journal.)

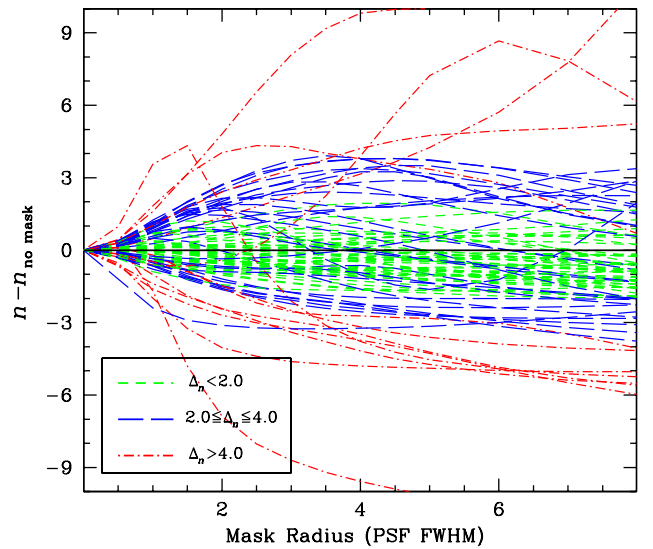


**Figure 35.** Effect of a central mask on the best-fitting Sérsic index for single-component fits of the elliptical galaxy sample. Each object is fit with circular masks of different radii, ranging from 0.8 to 8 times the PSF FWHM. While large systematic differences exist between models with and without a central mask, in general the fits are stable for masks with radii  $\gtrsim 2$  times FWHM of the PSF.

(A color version of this figure is available in the online journal.)

with different initial parameters but otherwise following our standard procedures for CGS. We refrain from fitting three-component models to the SDSS data because they have lower resolution. Despite the very different characteristics of the two data sets, we find that the fits produce very similar and consistent results, both in terms of the image residuals and in recovering basic parameters, as illustrated in Figure 34.

## APPENDIX D

### CENTRAL MASK

To decide on the appropriate size for the central mask, a series of single-component Sérsic models is fit to each elliptical galaxy, adopting central masks with different sizes ranging from 0.5 to 8 times the FWHM of the PSF. The result is shown in Figure 35, where the relative change of the Sérsic index is plotted against the size of the central mask. It is apparent that for most elliptical

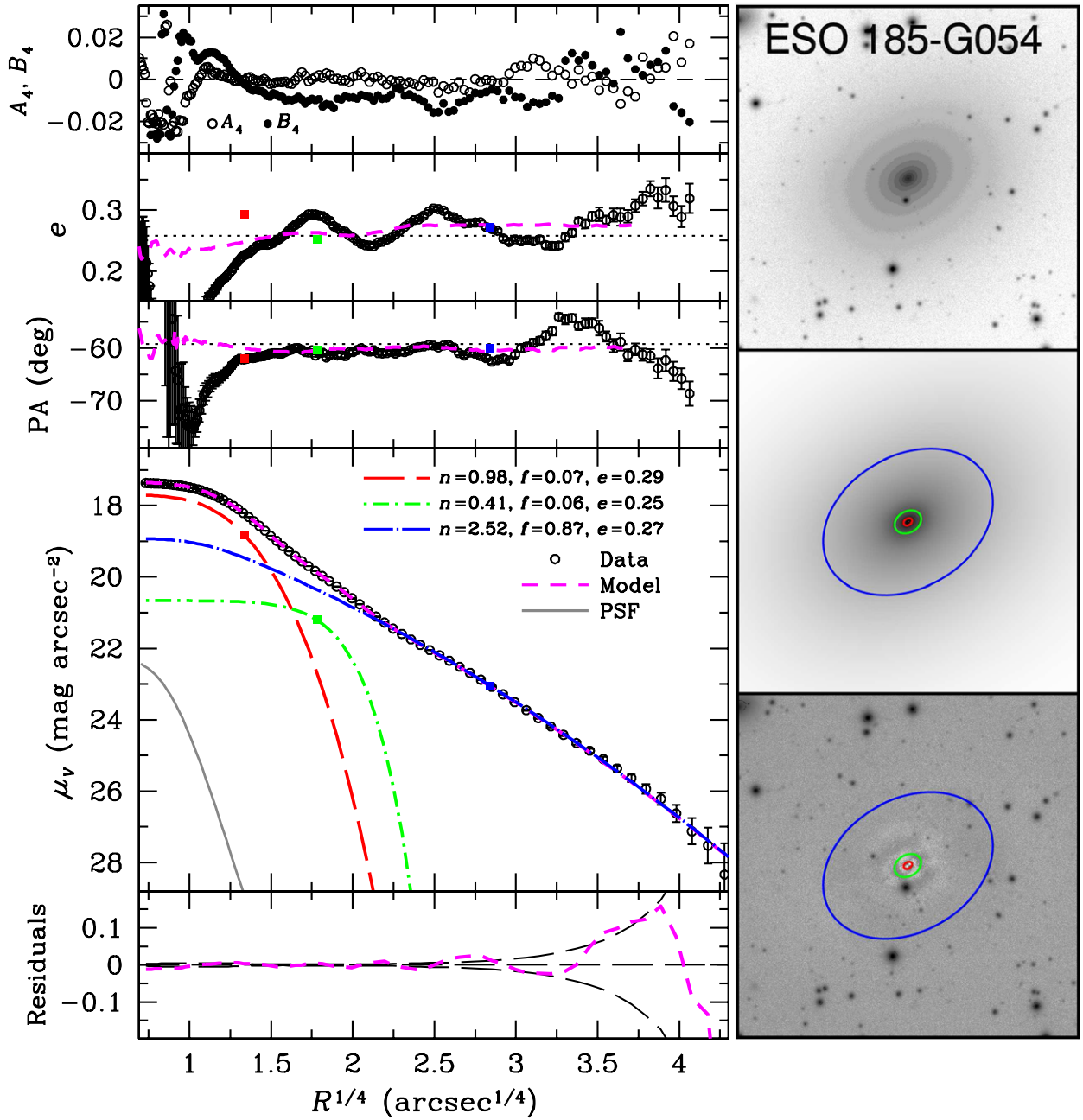


Figure 36. Best-fit model of ESO 185-G054. See Figure 5 for details.

(A color version and the complete figure set (93 images) are available in the online journal.)

galaxies the change of the Sérsic index is on average much weaker for radii beyond  $2 \times \text{FWHM}$ , indicating a transition to the regime outside of which the seeing disk has much reduced influence. Based on this, we adopt a radius of  $2 \times \text{FWHM}$  for the central mask. It is also interesting to note that different galaxies respond differently to the central mask, and that the Sérsic index “profile” for a large fraction of the objects is not flat outside the seeing disk. Both of these phenomena point to the intrinsic complexity of the central regions for nearby elliptical galaxies.

## APPENDIX E ATLAS OF FINAL FITS

Figure 36 presents the atlas of the final fits for the 94 elliptical galaxies in CGS. The format and labeling conventions are the

same as those in Figures 5 and 6. The right panels display, from top to bottom, images of the original data, the best-fit model, and the residuals; each panel has a dimension of  $2 R_{50} \times 2 R_{50}$  and is centered on the nucleus. The left panels compare the 1D profiles of the data and the model; from top to bottom, we show the isophotal shape parameters  $A_4$  and  $B_4$ ,  $e$ , PA, and the residuals between the data and the model. The observed  $\mu$  profile is extracted with  $e$  and PA fixed to the average value of the galaxy (Paper II), which is indicated by the dotted line in the  $e$  and PA panels. Individual subcomponents, each extracted using the geometric parameters generated by GALFIT, are plotted with different line types and colors; the PSF is plotted with arbitrary amplitude. Colored squares on the  $e$ , PA, and  $\mu$  plots mark the ellipticity, PA, and effective surface brightness of each component. The same color scheme

is used in the gray-scale images, where the ellipses trace  $R_{50}$ ,  $e$ , and PA of each component. In the residual plot, the three black dashed lines indicate the position of zero residuals and the level of photometric error. We only display three sample pages for illustration; the full set of figures is available in the online version of the paper, as well as on the project Web site <http://cgs.obs.carnegiescience.edu>.

## REFERENCES

- Aceves, H., Velázquez, H., & Cruz, F. 2006, *MNRAS*, **373**, 632
- Aihara, H., Allende Prieto, C., An, D., et al. 2011, *ApJS*, **193**, 29
- Arnaboldi, M., Ventimiglia, G., Iodice, E., Gerhard, O., & Coccato, L. 2012, *A&A*, **545**, A37
- Bell, E. F., & de Jong, R. S. 2001, *ApJ*, **550**, 212
- Bell, E. F., McIntosh, D. H., Katz, N., & Weinberg, M. D. 2003, *ApJL*, **585**, L117
- Bender, R. 1988, *A&A*, **193**, L7
- Bender, R., Burstein, D., & Faber, S. M. 1992, *ApJ*, **399**, 462
- Bender, R., & Möllenhoff, C. 1987, *A&A*, **177**, 71
- Bertin, G., Ciotti, L., & Del Principe, M. 2002, *A&A*, **386**, 149
- Bezanson, R., van Dokkum, P. G., Tal, T., et al. 2009, *ApJ*, **697**, 1290
- Brodie, J. P., & Strader, J. 2006, *ARA&A*, **44**, 193
- Burstein, D., Bender, R., Faber, S., & Nolthenius, R. 1997, *AJ*, **114**, 1365
- Caon, N., Capaccioli, M., & D'Onofrio, M. 1993, *MNRAS*, **265**, 1013
- Caon, N., Capaccioli, M., & D'Onofrio, M. 1994, *A&AS*, **106**, 199
- Capaccioli, M. 1989, *World of Galaxies* (Le Monde des Galaxies; New York: Springer), 208
- Cappellari, M., di Serego Alighieri, S., Cimatti, A., et al. 2009, *ApJL*, **704**, L34
- Cappellari, M., Emsellem, E., Krajnović, D., et al. 2011a, *MNRAS*, **413**, 813
- Cappellari, M., Emsellem, E., Krajnović, D., et al. 2011b, *MNRAS*, **416**, 1680
- Carlberg, R. G. 1986, *ApJ*, **310**, 593
- Carter, D. 1978, *MNRAS*, **182**, 797
- Cassata, P., Giavalisco, M., Guo, Y., et al. 2010, *ApJL*, **714**, L79
- Cassata, P., Giavalisco, M., Guo, Y., et al. 2011, *ApJ*, **743**, 96
- Cenarro, A. J., & Trujillo, I. 2009, *ApJL*, **696**, L43
- Cimatti, A., Cassata, P., Pozzetti, L., et al. 2008, *A&A*, **482**, 21
- Cimatti, A., Daddi, E., Renzini, A., et al. 2004, *Natur*, **430**, 184
- Cimatti, A., Nipoti, C., & Cassata, P. 2012, *MNRAS*, **422**, L62
- Ciotti, L. 1991, *A&A*, **249**, 99
- Ciotti, L., & Bertin, G. 1999, *A&A*, **352**, 447
- Coccato, L., Arnaboldi, M., Gerhard, O., et al. 2010, *A&A*, **519**, A95
- Coccato, L., Gerhard, O., Arnaboldi, M., et al. 2009, *MNRAS*, **394**, 1249
- Côté, P., Piatek, S., Ferrarese, L., et al. 2006, *ApJS*, **165**, 57
- Daddi, E., Renzini, A., Pirzkal, N., et al. 2005, *ApJ*, **626**, 680
- Damjanov, I., McCarthy, P. J., Abraham, R. G., et al. 2009, *ApJ*, **695**, 101
- de Vaucouleurs, G. 1948, *AnAp*, **11**, 247
- de Vaucouleurs, G. 1953, *MNRAS*, **113**, 134
- de Vaucouleurs, G., de Vaucouleurs, A., Corwin, H. G., Jr., et al. 1991, *Third Reference Catalogue of Bright Galaxies* (New York: Springer) (RC3)
- de Zeeuw, P. T., Bureau, M., Emsellem, E., et al. 2002, *MNRAS*, **329**, 513
- Dhar, B. K., & Williams, L. L. R. 2012, *MNRAS*, **427**, 204
- Donzelli, C. J., Muriel, H., & Madrid, J. P. 2011, *ApJS*, **195**, 15
- Ebnetter, K., Davis, M., & Djorgovski, S. 1988, *AJ*, **95**, 422
- Emsellem, E., Cappellari, M., Krajnović, D., et al. 2007, *MNRAS*, **379**, 401
- Faber, S. M., & Jackson, R. E. 1976, *ApJ*, **204**, 668
- Faber, S. M., Tremaine, S., Ajhar, E. A., et al. 1997, *AJ*, **114**, 1771
- Fan, L., Lapi, A., De Zotti, G., & Danese, L. 2008, *ApJL*, **689**, L101
- Fasano, G., & Bonoli, C. 1989, *A&AS*, **79**, 291
- Ferrarese, L., Côté, P., Jordán, A., et al. 2006, *ApJS*, **164**, 334
- Ferrarese, L., & Merritt, D. 2000, *ApJL*, **539**, L9
- Ferrarese, L., van den Bosch, F. C., Ford, H. C., Jaffe, W., & O'Connell, R. W. 1994, *AJ*, **108**, 1598
- Franx, M., Illingworth, G., & Heckman, T. 1989, *AJ*, **98**, 538
- Gabor, J. M., & Davé, R. 2012, *MNRAS*, **427**, 1816
- Gebhardt, K., Bender, R., Bower, G., et al. 2000, *ApJL*, **539**, L13
- Gebhardt, K., Richstone, D., Ajhar, E. A., et al. 1996, *AJ*, **112**, 105
- Glass, L., Ferrarese, L., Côté, P., et al. 2011, *ApJ*, **726**, 31
- González, A. H., Zabludoff, A. I., & Zaritsky, D. 2005, *ApJ*, **618**, 195
- Goudfrooij, P., Hansen, L., Jorgensen, H. E., & Norgaard-Nielsen, H. U. 1994, *A&AS*, **105**, 341
- Graham, A. W., & Driver, S. P. 2005, *PASA*, **22**, 118
- Graham, A. W., Driver, S. P., Petrosian, V., et al. 2005, *AJ*, **130**, 1535
- Graham, A., Erwin, P., Trujillo, I., & Asensio Ramos, A. 2003, *AJ*, **125**, 2951
- Graham, A., Lauer, T. R., Colless, M., & Postman, M. 1996, *ApJ*, **465**, 534
- Greene, J. E., Murphy, J. D., Comerford, J. M., Gebhardt, K., & Adams, J. J. 2012, *ApJ*, **750**, 32
- Guo, Y., McIntosh, D. H., Mo, H. J., et al. 2009, *MNRAS*, **398**, 1129
- Häring, N., & Rix, H.-W. 2004, *ApJL*, **604**, L89
- Harms, R. J., Ford, H. C., Tsvetanov, Z. I., et al. 1994, *ApJL*, **435**, L35
- Hjorth, J., & Madsen, J. 1995, *ApJ*, **445**, 55
- Ho, L. C., Li, Z.-Y., Barth, A. J., Seigar, M. S., & Peng, C. Y. 2011, *ApJS*, **197**, 21 (Paper I)
- Hopkins, P. F., Cox, T. J., Dutta, S. N., et al. 2009a, *ApJS*, **181**, 135
- Hopkins, P. F., Hernquist, L., Cox, T. J., Kereš, D., & Wykts, S. 2009b, *ApJ*, **691**, 1424
- Hopkins, P. F., Lauer, T. R., Cox, T. J., Hernquist, L., & Kormendy, J. 2009c, *ApJS*, **181**, 486
- Hoyos, C., den Brok, M., Verdoes Kleijn, G., et al. 2011, *MNRAS*, **411**, 2439
- Jaffe, W., Ford, H. C., O'Connell, R. W., van den Bosch, F., & Ferrarese, L. 1994, *AJ*, **108**, 1567
- Je drzejewski, R. I. 1987, *MNRAS*, **226**, 747
- Johansson, P. H., Naab, T., & Ostriker, J. P. 2012, *ApJ*, **754**, 22
- Khochfar, S., Emsellem, E., Serra, P., et al. 2011, *MNRAS*, **417**, 845
- Kim, M., Ho, L. C., Peng, C. Y., et al. 2008, *ApJ*, **687**, 767
- King, I. R. 1978, *ApJ*, **222**, 1
- Kormendy, J. 1977, *ApJ*, **218**, 333
- Kormendy, J. 1982, in *Morphology and Dynamics of Galaxies*, ed. L. Martinet & M. Mayor (Sauverny: Geneva Obs.), 113
- Kormendy, J. 1985, *ApJL*, **292**, L9
- Kormendy, J., & Bender, R. 2012, *ApJS*, **198**, 2
- Kormendy, J., Fisher, D. B., Cornell, M. E., & Bender, R. 2009, *ApJS*, **182**, 216 (K09)
- Kormendy, J., & Richstone, D. O. 1995, *ARA&A*, **33**, 581
- Kuntschner, H. 2000, *MNRAS*, **315**, 184
- La Barbera, F., de Carvalho, R. R., de la Rosa, I. G., et al. 2010, *AJ*, **140**, 1528
- Larson, R. B. 1974, *MNRAS*, **166**, 585
- Lauer, T. R. 1985, *ApJ*, **292**, 104
- Lauer, T. R., Ajhar, E. A., Byun, Y.-I., et al. 1995, *AJ*, **110**, 2622
- Lauer, T. R., Gebhardt, K., Faber, S. M., et al. 2007, *ApJ*, **664**, 226
- Laurikainen, E., Salo, H., Buta, R., Knapen, J. H., & Comerón, S. 2010, *MNRAS*, **405**, 1089
- Ledo, H. R., Sarzi, M., Dotti, M., Khochfar, S., & Morelli, L. 2010, *MNRAS*, **407**, 969
- Li, Z.-Y., Ho, L. C., Barth, A. J., & Peng, C. Y. 2011, *ApJS*, **197**, 22 (Paper II)
- Lima Neto, G. B., Gerbal, D., & Márquez, I. 1999, *MNRAS*, **309**, 481
- Magorrian, J., Tremaine, S., Richstone, D., et al. 1998, *AJ*, **115**, 2285
- Malin, D. 1979, *Natur*, **277**, 279
- Malin, D. F., & Carter, D. 1980, *Natur*, **285**, 643
- Malin, D. F., & Carter, D. 1983, *ApJ*, **274**, 534
- McCarthy, P. J., Le Borgne, D., Crampton, D., et al. 2004, *ApJL*, **614**, L9
- McConnell, N. J., Ma, C.-P., Gebhardt, K., et al. 2011, *Natur*, **480**, 215
- McConnell, N. J., Ma, C.-P., Murphy, J. D., et al. 2012, *ApJ*, **756**, 22
- Michard, R. 2002, *A&A*, **384**, 763
- Morgan, W. W., & Lesh, J. R. 1965, *ApJ*, **142**, 1364
- Murphy, J. D., Gebhardt, K., & Adams, J. J. 2011, *ApJ*, **729**, 129
- Naab, T., Johansson, P. H., & Ostriker, J. P. 2009, *ApJL*, **699**, L178
- Naab, T., Johansson, P. H., Ostriker, J. P., & Efstathiou, G. 2007, *ApJ*, **658**, 710
- Naab, T., & Trujillo, I. 2006, *MNRAS*, **369**, 625
- Nieto, J.-L., Bender, R., Poulain, P., & Surma, P. 1992, *A&A*, **257**, 97
- Nipoti, C., Londrillo, P., & Ciotti, L. 2006, *MNRAS*, **370**, 681
- Nipoti, C., Treu, T., Leauthaud, A., et al. 2012, *MNRAS*, **422**, 1714
- Oemler, A., Jr. 1974, *ApJ*, **194**, 1
- Onodera, M., Arimoto, N., Daddi, E., et al. 2010, *ApJ*, **715**, 385
- Oser, L., Naab, T., Ostriker, J. P., & Johansson, P. H. 2012, *ApJ*, **744**, 63
- Oser, L., Ostriker, J. P., Naab, T., Johansson, P. H., & Burkert, A. 2010, *ApJ*, **725**, 2312
- Papovich, C., Bassett, R., Lotz, J. M., et al. 2012, *ApJ*, **750**, 93
- Peletier, R. F., Davies, R. L., Illingworth, G. D., Davis, L. E., & Cawson, M. 1990, *AJ*, **100**, 191
- Peng, C. Y., Ho, L. C., Impey, C. D., & Rix, H.-W. 2002a, *AJ*, **124**, 266
- Peng, C. Y., Ho, L. C., Impey, C. D., & Rix, H.-W. 2010, *AJ*, **139**, 2097
- Peng, E. W., Ford, H. C., Freeman, K. C., & White, R. L. 2002b, *AJ*, **124**, 3144
- Pota, V., Forbes, D. A., Romanowsky, A. J., et al. 2013, *MNRAS*, **428**, 389
- Ravindranath, S., Ho, L. C., Peng, C. Y., Filippenko, A. V., & Sargent, W. L. W. 2001, *AJ*, **122**, 653
- Rembold, S. B., Pastoriza, M. G., Ducati, J. R., Rubio, M., & Roth, M. 2002, *A&A*, **391**, 531
- Romanowsky, A. J., Strader, J., Brodie, J. P., et al. 2012, *ApJ*, **748**, 29
- Sandage, A., & Bedke, J. 1994, *The Carnegie Atlas of Galaxies* (Washington, DC: Carnegie Inst. of Washington)

- Sandage, A. R., & Tammann, G. A. 1981, A Revised Shapley-Ames Catalog of Bright Galaxies (Washington, DC: Carnegie Inst. of Washington)
- Schombert, J. M. 1986, *ApJS*, **60**, 603
- Schweizer, F. 1980, *ApJ*, **237**, 303
- Schweizer, F. 1982, *ApJ*, **252**, 455
- Seigar, M. S., Graham, A. W., & Jerjen, H. 2007, *MNRAS*, **378**, 1575
- Sérsic, J. L. 1968, Atlas de Galaxias Australes (Córdoba: Obs. Astron., Univ. Nac. Córdoba)
- Shen, S., Mo, H. J., White, S. D. M., et al. 2003, *MNRAS*, **343**, 978
- Szomoru, D., Franx, M., & van Dokkum, P. G. 2012, *ApJ*, **749**, 121
- Tal, T., van Dokkum, P. G., Nelan, J., & Bezanson, R. 2009, *AJ*, **138**, 1428
- Toft, S., van Dokkum, P., Franx, M., et al. 2007, *ApJ*, **671**, 285
- Tomita, A., Aoki, K., Watanabe, M., Takata, T., & Ichikawa, S. 2000, *AJ*, **120**, 123
- Tran, H. D., Tsvetanov, Z., Ford, H. C., et al. 2001, *AJ*, **121**, 2928
- Trujillo, I., Erwin, P., Ramos, A. A., & Graham, A. W. 2004, *AJ*, **127**, 1917
- Trujillo, I., Feulner, G., Goranova, Y., et al. 2006, *MNRAS*, **373**, L36
- Trujillo, I., Graham, A. W., & Caon, N. 2001, *MNRAS*, **326**, 869
- van Albada, T. S. 1982, *MNRAS*, **201**, 939
- van de Sande, J., Kriek, M., Franx, M., et al. 2011, *ApJL*, **736**, L9
- van der Wel, A., Bell, E. F., van den Bosch, F. C., Gallazzi, A., & Rix, H.-W. 2009, *ApJ*, **698**, 1232
- van der Wel, A., Holden, B. P., Zirm, A. W., et al. 2008, *ApJ*, **688**, 48
- van Dokkum, P. G., Franx, M., Kriek, M., et al. 2008, *ApJL*, **677**, L5
- van Dokkum, P. G., Kriek, M., & Franx, M. 2009, *Natur*, **460**, 717
- van Dokkum, P. G., Whitaker, K. E., Brammer, G., et al. 2010, *ApJ*, **709**, 1018
- Williams, R. J., Quadri, R. F., & Franx, M. 2011, *ApJL*, **738**, L25
- Wu, H., Shao, Z., Mo, H. J., Xia, X., & Deng, Z. 2005, *ApJ*, **622**, 244
- Yoon, I., Weinberg, M. D., & Katz, N. 2011, *MNRAS*, **414**, 1625
- Zaritsky, D., González, A. H., & Zabludoff, A. I. 2006, *ApJ*, **638**, 725
- Zibetti, S., Charlot, S., & Rix, H.-W. 2009, *MNRAS*, **400**, 1181
- Zibetti, S., White, S. D. M., Schneider, D. P., & Brinkmann, J. 2005, *MNRAS*, **358**, 949